Cite as: R. C. Bretherton et al., Science 10.1126/science.adv9157 (2025).

Preventing hypocontractility-induced fibroblast expansion alleviates dilated cardiomyopathy

Ross C. Bretherton^{1,2,3}, Isabella M. Reichardt^{1,2,3}, Kristin A. Zabrecky^{2,3,4}, Abigail Nagle^{1,2,3}, Logan R. J. Bailey^{2,3,5}, Darrian Bugg^{2,3,5}, Sasha Smolgovsky^{2,3,5}, Amy L. Gifford^{2,3,5}, Timothy S. McMillen^{1,6}, Alex J. Goldstein^{2,5}, Kristina B. Kooiker^{2,3,7}, Galina V. Flint¹, Amy Martinson^{2,3,5}, Jagdambika Gunaje^{2,3,5}, Franziska Koser⁸, Elizabeth Plaster^{2,3,5}, Wolfgang A. Linke⁸, Michael Regnier^{1,2,3,9}, Farid Moussavi-Harami^{2,3,5,7,9}, Nathan J. Sniadecki^{1,2,3,5,9,10}, Cole A. DeForest^{1,2,11,12,13,14}, Jennifer Davis^{1,2,3,5,9*}

¹Department of Bioengineering, University of Washington, Seattle, WA, USA. ²Institute for Stem Cell and Regenerative Medicine, University of Washington, Seattle, WA, USA. ³Center for Cardiovascular Biology, University of Washington, Seattle, WA, USA. ⁴Department of Comparative Medicine, University of Washington, Seattle, WA, USA. Department of Lab Medicine and Pathology, University of Washington, Seattle, WA, USA. Department of Anesthesiology, University of Washington, Seattle, WA, USA. PDivision of Cardiology, University of Washington, Seattle, WA, USA. Institute of Physiology II, University of Münster, Germany. Center for Translational Muscle Research, University of Washington, Seattle, WA, USA. 10 Department of Mechanical Engineering, University of Washington, Seattle, WA, USA. ¹¹Department of Chemical Engineering, University of Washington, Seattle, WA, USA. ¹²Department of Chemistry, University of Washington, Seattle, WA, USA. 13 Molecular Engineering & Sciences Institute, University of Washington, Seattle, WA, USA. 14 Institute for Protein Design, University of Washington, Seattle, WA, USA. *Corresponding author. Email: jendavis@uw.edu

Cardiomyocyte hypocontractility underlies inherited dilated cardiomyopathy (DCM). Yet, whether fibroblasts modify DCM phenotypes remains unclear despite their regulation of fibrosis, which strongly predicts disease severity. Expression of a hypocontractility-linked sarcomeric variant in mice triggered cardiac fibroblast expansion from the de novo formation of hyperproliferative-mechanosensitized fibroblast states, which occurred prior to eccentric myocyte remodeling. Initially this fibroblast response reorganized fibrillar collagen and stiffened the myocardium albeit without depositing fibrotic tissue. These adaptations coincided with heightened matrix-integrin receptor interactions and diastolic tension sensation at focal adhesions within fibroblasts. Targeted p38 deletion arrested these cardiac fibroblast responses in DCM mice, which prevented cardiomyocyte remodeling and improved contractility. In conclusion, p38-mediated fibroblast responses were essential regulators of DCM severity, marking a potential cellular target for therapeutic intervention.

Dilated cardiomyopathy (DCM) is a leading cause of heart failure worldwide, which arises from a cadre of insults including inherited mutations in contractile or structural proteins expressed in cardiomyocytes (1-3). The clinical hallmarks of DCM are reduced systolic function, myocardial thinning, left ventricular chamber dilation, and fibrosis. Despite a robust prevalence of DCM in the population, there are limited treatment options and, as of yet, no cure (3–6). Potential pharmaceuticals for DCM such as myosin modulators have underperformed at fully correcting the DCM phenotype, especially established fibrosis in mice and clinical trials, thus tempering their therapeutic value (2, 7, 8). This absence of fully effective treatments may be due to a decades long struggle with mechanistically linking the primary contractile defect to variable DCM phenotypes (9).

Common to most severe DCM phenotypes is fibrosis, which often precedes and exacerbates cardiac structural remodeling (10-12). Remodeling of the heart's extracellular matrix (ECM), such as during the fibrotic response to stress, is primarily regulated by resident fibroblasts of the Tcf21 and Pdgfra lineages (13– 16). While cardiac fibroblasts can be activated chemically to secrete fibrotic ECM, these cells are also highly sensitive to mechanical signals including substrate stiffness, alignment, and stretch (17). Fibroblasts are posited to function within mechanical feedback loops by structurally and biochemically tuning the

extracellular environment's material properties to maintain a tissue's preferred mechanical state (18). Given fibroblasts are physically coupled to cardiomyocytes via the ECM (19), it was hypothesized that in DCM driven by myocyte hypocontractility cardiac fibroblasts act as tissue-scale mechanical rheostats that sense impaired myocyte force generation and then adaptively remodel the extracellular environment to maintain mechanical homeostasis. We further propose that these adaptive fibroblast responses are essential secondary drivers of DCM phenotype and disease severity.

Results

Prior to myocyte growth, hypocontractile sarcomeres induce myocardial stiffening related to collagen reorganization.

Sarcomeric hypocontractility was modeled in mice by expressing an experimentally-derived I61Q variant of cardiac troponin C (cTnC) specifically in cardiomyocytes using a doxycycline-repressible α-myosin heavy chain promoter [fig. S1A (1)]. The I61Q mutation lowers cTnC's Ca²⁺ binding affinity and hence reduces force production on a beat-to-beat basis (20, 21). This change is apparent by echocardiography, which showed reduced ejection fraction in the hearts of I61Q transgenic mice by 2 months of age relative to the control (CON) group, which consisted of non-transgenic and tetracycline transactivator (tTA) transgenic littermates

(fig. S1B). These two genotypes were merged into a single control group, because previous studies showed no effects of the tTA transgene (1). The time frame of dilated remodeling was defined by morphologic measurements of isolated CON and I61Q myocytes in the presence of a myosin inhibitor blebbistatin, which ensures the cellular dimensions represent structural changes rather than sarcomere elongation from I61Q cTnC-dependent desensitization of the myofilaments to Ca²⁺ (1). At 2 months of age I61Q myocytes had normal lengths and length: width ratios when compared to CON indicating a lack of structural remodeling (Fig. 1, A and B). However, by 4 months I61Q myocytes were longer and had greater length: width ratios- a structural hallmark of eccentric hypertrophy and DCM [Fig. 1, A and B (22, 23)]. Consistent with this progressive increase in I61Q myocyte length from serial sarcomere addition (24), heart weight to body weight ratios were similar to CON at 2 months of age but significantly increased by 4 (Fig. 1C; P < 0.001). By contrast, diastolic chamber dimensions as measured by echocardiography were increased at both ages (Fig. 1D). This discrepancy between myocyte and organ level dilation in I61Q mice could stem from altered diastolic tone driven by Ca2+ desensitized myofilaments that lower crossbridge attachment at diastolic [Ca²⁺]. This hypothesis was examined by measuring sarcomere lengths in isolated myocytes from 2-month-old I61Q and CON mice at diastolic [Ca2+] (1). As expected I61Q myocytes had longer resting sarcomere lengths (Fig. 1E). Organ level dilation could also be caused by myocardial stiffness, considering genotype positive cardiomyopathy patients can have stiffer hearts prior to the onset of structural remodeling (9-11). Indeed, a hemodynamic index of cardiac stiffness, end diastolic pressure-volume relationship (EDPVR), was elevated in 2-month-old I61Q mice and worsened with age (Fig. 1F). To determine if myocardial or ECM stiffness caused heightened EDPVR in I61Q mice, the passive mechanical properties of intact and decellularized hearts were measured using a Langendorff working heart preparation that lacked electrical stimulation (fig. S1, C and D). Here, intact hearts from I61Q transgenic and CON mice were subjected to retrograde perfusion with Krebs-Henseleit buffer containing blebbistatin to negate any stiffness from attached crossbridges, and then a balloon was inserted into the left ventricle for volumetric inflation of the chamber in a stepwise manner (Fig. 1G and fig. S1C). The balloon pressure was recorded during each inflation step, which exhibited a maximal pressure required to achieve the initial volume change followed by a gradual decrease in pressure due to viscoelastic relaxation (Fig. 1G). Following intact measurements, hearts were decellularized and the assay repeated to measure passive mechanical properties of the ECM in the same preparation. Both intact and decellularized preparations from 161Q mice required higher maximal pressures per inflation, indicating both the myocardium and ECM are stiffer relative to CON (Fig. 1, H and I, and fig. S1, C and D).

Titin isoforms and post-translational modifications were

surveyed by Western blot given their regulation of myocyte passive stiffness in the physiologic range (25). The stiffer N2B isoform was up-regulated in I61Q hearts (Fig. 1J and fig.S1E), whereas post translational modifications of titin that enhance myocyte compliance were reduced as shown by the lack of phosphorylation at serine residues in the N2B-specific sequence (S267P) and PEVK region (S26P) when compared to CON [Fig. 1, K and L, and fig. S1E (26, 27)]. While titin composition was altered in I61Q cardiomyocytes, the modest effect size prompted examination of the ECM's biochemical composition, quantity, and organization to determine additional causes of stiffness in I61Q hearts (20). Label-free data-independent acquisition (DIA) mass spectrometry (MS) of decellularized cardiac ECM from I61Q cTnC transgenic and CON mice was performed (Fig. 1M and fig. S2, A to P) and recovered ~72% of core collagens, ECM glycoproteins, and proteoglycans (28). The relative abundance of primary ECM constituents was largely unchanged between genotypes (~6% of the matrisome; Fig. 1M and fig. S2A). Only 22 core matrisome proteins were differentially expressed between CON and I61Q mice, including several laminin subtypes and type 6 collagen (Fig. 1M), an established biomarker of heart failure not yet linked to ECM stiffening (28–30). Closer examination of collagen abundance with less stringent p-values (p<0.05) showed several fibrillar collagens starting to increase in I61Q cardiac ECM but only network forming collagens 6a and 8a were statistically different (fig. S2B). This matches histologic analysis of fibrosis by picrosirius red staining, in which no differences were detected between groups at this age (Fig. 1, N and O). By 4 months, I61Q transgenics began accruing interstitial cardiac fibrosis concomitant with the structural lengthening of myocytes (Fig. 1, A to C and N and O). The MS data were also used to detect covalent and non-covalent crosslinking of fibrillar collagens as a mechanism for ECM stiffness. Of the few glycation sites identified, none were different between genotypes (fig. S2, C to E). By contrast, we found that a smaller proportion of I61Q fibrillar collagens had hydroxylated proline and lysine residues, with the biggest decrease being reduced abundance of hydroxylated lysines in COL1A1 (fig. S2, F to I). Reduced proline and lysine hydroxylation on fibrillar collagens is typically associated with ECM instability and immaturity (31-33), and collagen birefringence imaging showed a greater proportion of collagen fibers were immature in I61Q versus control ECM (fig. S2Q). No differences in ECM crosslinking enzyme abundance were detected (fig. S2, J to P), suggesting crosslinking wasn't responsible for stiffer ECM in I61Q mice. Multiscale reorganization of collagen fibers was also explored as a causal mechanism for ECM stiffness (34). Second harmonic generation (SHG) microscopy and imaging of decellularized I61Q and CON hearts below the epicardial surface identified increased collagen fiber alignment in the circumferential-longitudinal plane (Fig. 1, P to S), which is consistent with findings linking collagen fiber alignment to heightened anisotropic strength and stiffness (35, 36). There was no significant difference

in collagen fiber length between controls and I61Q ECM preparations (Fig. 1R), indicating the observed topographical changes were not simply a product of collagen elongation. Because smaller collagen fibril diameter and increased packing also enhance ECM strength and passive stiffness (37–39), transmission electron microscopy (TEM) was used to examine collagen fiber ultrastructure. Indeed, I61Q collagen fibrils had smaller diameters and cross-sectional areas with a greater packing density relative to controls (Fig. 1, T to V, and fig. S2R). The proteoglycan decorin, which restrains collagen fibril diameter and creates denser networks similar to these findings (40, 41), was more abundant in I61Q ECM (Fig. 1W). These data suggest the structural organization of fibrillar collagen rather than quantity, composition, or crosslinking underlies the passive ECM stiffness in I61Q hearts.

Fibroblast expansion promotes early cardiac stiffening and collagen reorganization.

Typically, tissue stiffness initiates cardiac fibroblast activation and transition to a myofibroblast state, a cellular process required for fibrotic ECM production (42, 43). Activated myofibroblasts were measured in myocardial sections from 2-month-old I61Q cTnC and CON mice by quantifying the number of cells that were positive for both the myofibroblast marker smooth muscle α -actin (αSMA) and quiescent fibroblast marker platelet-derived growth factor receptor α (PDGFRα). No fibroblast-to-myofibroblast conversion was evident even after the onset of fibrosis in I61Q hearts (Fig. 2, A and B). The competence of I61Q cardiac fibroblasts to activate was also examined in vitro by stimulating them with recombinant TGF\$1 and calculating the percentage of the population that had formed α SMA-positive stress fibers (4). This assay revealed no differences between genotypes at baseline or in response to TGFβ1, suggesting cardiac fibroblasts from I61Q transgenics are capable of differentiating into myofibroblasts and possess equal sensitivity to activating ligands as CON (fig. S3, A and B). Previous single-cell RNA sequencing (RNA-seq) studies have demonstrated that αSMA positive fibroblasts comprise only a small fraction of the activated myofibroblast population, whereas periostin (Postn) expression marks all activated myofibroblast states (44). To determine if I61Q fibroblasts are canonically activating but not transitioning to mature αSMA+ states, Postn lineage tracing was performed in I61Q transgenic and CON mice using a Cre-regulated dual color fluorescent reporter and tamoxifen (TAM) inducible Postn-Cre-driver (Postni^{Cre}-mT/mG, (15, 45, 46)). Postn lineage tracing detected small pockets of activated Postn⁺ cells in the interstitium and adventitia of I61Q hearts but only at 8 months of age, which matches the start of decompensation [Fig. 2, A (right) and C, and fig. S3, C and D] (2). These results suggest that (i) the typical fibrotic process of myofibroblast formation only occurs in hypocontractility-induced DCM once the heart is failing and that (ii) fibroblast activation to an intermediate or fully matured myofibroblast state is not essential for ECM and

First release: 11 September 2025

myocardial stiffening.

To determine the basis for this myofibroblast-independent cardiac stiffening, single-nuclei RNA-seq (snRNA-seq) of 2-monthold CON and I61Q hearts were analyzed for the emergence of atypical fibroblast states (Fig. 2D). Five fibroblast substates were identified by hierarchical clustering of differentially expressed genes with each cluster expressing Col1a1 and Col1a2 at varying levels (Fig. 2, D to F). Cluster 1 and 3 fibroblasts were rare in controls but expanded in I61Q hearts (Fig. 2, D and E, and fig. S3E). These clusters were defined by transcripts involved in mechanotransduction (ECM-receptor, focal adhesion, and adherens junctions) and cell cycle/chromatin segregation, respectively (Fig. 2G and table S1). Independent bulk RNA-seq analysis of PDGFRα purified cardiac fibroblasts validated these findings with greater sequencing depth. Here 363 up-regulated genes and 449 downregulated genes were identified in I61Q fibroblasts (Fig. 2H, fig. S3F, and data S1). Genes with the largest change in expression included a variety of cell cycle regulators such as cyclin genes (Ccnb1, Ccnb2, Ccnd1, Ccne2, Ccnf), cyclin-dependent kinase 1 (Cdk1), marker of proliferation Ki67 (Mki67), and aurora kinase (Aurka) (Fig. 2H, fig. S3F, and data S1). To assess whether altered levels of cell cycle markers led to heightened proliferation and expansion of I61Q fibroblasts, cardiac sections from postnatal day 14 (p14), 1- and 2-month-old mice were stained for the fibroblast marker PDGFRα and cell cycle marker phospho-histone H3 (pHH3; Fig. 2, I to M), which demonstrated that fibroblasts in I61Q myocardial sections had heightened proliferation signals beginning at 2-months when CON fibroblasts are quiescent (47). In accordance with heightened cell cycle activity PDGFR α^+ fibroblast density doubled and remained at this level in I61Q hearts throughout the course of disease despite a decline in cell cycle activity at 4 months of age (Fig. 2, I and J, and fig. S3G), suggesting steadystate was reached with regards to fibroblast expansion. To determine if immune cell activation was associated with cardiac fibroblast proliferation, myocardial sections were analyzed at the 2 month timepoint for cardiac-infiltrating CD11b+ myeloid and CD4+ T cells, which have known pro-fibrotic roles in other etiologies of heart failure. These histologic methods showed CON and I61Q hearts had similar immune profiles, suggesting crosstalk with immune cells wasn't driving proliferation (fig. S3, H to K). This I61Q cTnC-dependent expansion of the fibroblast population coincided with up-regulated Col1a1, 1a2, and 3a1 transcripts and downregulation of key ECM degrading enzymes like metalloproteinases (Mmp and Adamts) and cathepsins (Cts), which together should have promoted fibrotic tissue deposition (fig. S3, L to Q). As this was not observed in I61Q hearts (Fig. 1, M to O, and fig. S2B), we reasoned that post-transcriptional fibrillar collagen immaturity (fig. S2, F to I and Q) restrained the fibrotic response despite the expanded fibroblast population.

While fibrillar collagen deposition is a common fibroblast-dependent mechanism underlying tissue stiffening, increased cell

density and cumulative traction forces exerted by the expanded fibroblast population in I61Q could also contribute myocardial stiffening and circumferential ECM alignment, as observed with progressive volume overload linked to DCM (48). Indeed, hyperproliferative I61Q fibroblasts compacted the surrounding ECM to a greater extent than those from CON hearts following encapsulation in free-floating collagen gels (Fig. 2, N and O). To test whether proliferation was essential to gel compaction, a smallmolecule cyclin-dependent kinase inhibitor (CDKi) dinaciclib was delivered in the culture media. CDKi treatment reduced proliferation of cardiac fibroblasts from both genotypes to similarly low levels and blocked genotype-dependent gel compaction (Fig. 2, N to P), demonstrating increased fibroblast numbers rather than greater cell contraction caused compaction. To further confirm that gel compaction was due to proliferation rather than ECM degradation, a set of cell-laden collagen gels were also treated with marimastat, a broad-spectrum inhibitor of matrix metalloproteinases, which had no effect on I61Q fibroblast proliferation or gel compaction for either fibroblast genotype (fig. S3, R to T). Similar to the collagen gels, fibrin tissues seeded with cardiac fibroblasts from I61Q transgenic hearts had increased compaction and generated more passive tension than those seeded with CON cardiac fibroblasts as measured by polydimethylsiloxane (PDMS) after deflection (Fig. 2, Q to S). Concomitant with the heightened passive tension, I61Q fibroblasts were more aligned within the tissues, suggesting fibroblast proliferation contributes to myocardial stiffness and alignment (Fig. 2T).

Stiffening of cardiomyocytes and altered preload from I61Qdependent hypocontractility could also produce the traction needed to align and lengthen collagen fibers. To study the acute effects of I61Q cTnC on tissue alignment and stiffening in the absence of hemodynamic load, naïve neonatal rat cardiomyocytes were seeded into engineered heart tissues (EHTs) mounted on PDMS posts and adenovirally transduced with FLAG-tagged I61Q cTnC (AdI61Q) or wild-type cTnC (AdWT) as a control. After 2 weeks of culture, AdI61Q EHTs functionally phenocopied the I61Q transgenic mice (2), including reduced twitch force and hypocontractility (Fig. 2, U and V). Notably absent from the I61Q EHT phenotype was any difference in passive tension generation or tissue alignment (Fig. 2, W and X), which differs from tissues engineered with cardiac fibroblasts from I61Q transgenic mice (Fig. 2, Q to T). Taken together these experiments demonstrate that in the absence of fibroblast-generated passive tension and/or hemodynamic loading, I61Q cTnC expression by the cardiomyocyte alone is insufficient to align and stiffen myocardial tissues in vitro.

Sarcomere hypocontractility-induced ECM interactions and heightened diastolic tension sensation promote fibroblast proliferation.

Cellular crosstalk that might drive the hyperproliferative phenotype of I61Q cardiac fibroblasts was interrogated by performing

First release: 11 September 2025

ligand-receptor analysis of myocyte and fibroblast clusters identified by snRNA-seq (Figs. 2D and 3A). Seventeen ligand-receptor pairs of varying strengths were identified where receptors were expressed by fibroblasts and ligands expressed by myocytes (Fig. 3A). Ligand-receptor analysis of immune cell-fibroblast and endothelial cell-fibroblast pairs showed minimal overlap with myocyte-fibroblast interactions except for Ccn1/Sdc4 and Adam9/Itgb1 (Fig. 3A and fig. S4, A and B), suggesting myocytefibroblast communicate via discrete signals. Of those myocyte-fibroblast interactions 6 were strongly altered in I61Q hearts (Fig. 3A). Most of these communication pathways involved ECMreceptor pairs that included Col4a5/Ddr1, Col4a2/Ddr1, Col4a3/Itga11+Itgb1, Col4a3/Itga1+Itgb1, Adam9/Itga3+Itgb1 (Fig. 3A). To examine whether these ECM interactions induced fibroblast proliferation in equivalent mechanical environments, cardiac fibroblasts were encapsulated in poly(ethylene glycol) (PEG)-based hydrogels (~2 kPa storage modulus) that were covalently decorated with pepsin-digested ECM from CON or I61Q hearts and functionalized with 4-azidobutyric acid N-hydroxysuccinimide ester (36, 37). CON ECM hydrogels lowered I61Q cardiac fibroblast proliferation to CON levels, whereas hydrogels containing I61Q ECM maintained the heightened proliferation of I61Q fibroblasts but also increased CON cell cycle activity to I61Q levels (Fig. 3B). To isolate which ECM ligands drive proliferation 36 combinations of ECM proteins contained in soft (~10 kPa) polyacrylamide gels were screened with naïve CON cardiac fibroblasts. Here, type 4 and 6 collagen caused the greatest increase in proliferation relative to other ECM substrates (Fig. 3C). COL6A was enriched in I61Q ECM proteomics (Fig. 1M and fig. S2B) and Col4a was identified as a ligand-receptor pair exclusively in I61Q hearts (Fig. 3A), suggesting matrix signals are advancing the DCM phenotype. Since some modestly enriched secreted factor-receptor pairs were identified in I61Q hearts (Fig. 3A), additional experiments were performed to rule out myocyte secreted factors as causal for the I61Q fibroblast phenotype. Here, naive CON cardiac fibroblasts cultured in conditioned media from 2- or 4-month-old CON or I61Q myocytes showed no difference in the number of proliferating fibroblasts with any of the treated or control conditions (fig. S4C). Similarly, collagen gels seeded with CON cardiac fibroblasts and treated with conditioned media from 2-month-old CON or I61Q myocytes had slightly enhanced collagen gel compaction, but no genotype-dependent differences (fig. S4D). These data support ECM-ligand interactions rather than myocyte secreted factors as drivers of fibroblast expansion in I61Q hearts.

Because these findings pinpoint ECM-receptor interactions, a coculture assay was developed to determine whether cardiac fibroblast focal adhesions sense different mechanical signals in an I61Q versus CON cardiomyocyte environment. For this assay CON cardiac fibroblasts were genetically modified with a FRET-based vinculin tension sensor and sparsely seeded on top of neonatal

myocyte monolayers that were adenovirally transduced with either I61Q or wild-type cTnC (Fig. 3D). Fibroblast focal adhesion FRET efficiency was measured as a surrogate for force when the myocytes were under fully relaxed (+blebbistatin), diastolic [Ca²⁺ concentration (pCa) 6.0], or submaximally activated (pCa 5.2) conditions (Fig. 3, E to G). Fibroblasts sensed heightened focal adhesion tension in the I61Q myocyte environment when the cardiomyocytes were either completely relaxed (Fig. 3E) or in diastolic Ca²⁺ conditions (Fig. 3F). Notably, focal adhesions tension sensations were similar between genotypes in submaximally activated conditions despite the presence of I61Q-expressing myocytes (Fig. 3G), indicating cardiac fibroblast focal adhesions differentially sense passive tension in I61Q myocytes that results from hypocontractility and stiffer titin isoforms rather than the forces generated during active contraction. This elevated passive tension sensation is consistent with (i) up-regulated ECMreceptor/focal adhesion genes in fibroblast states unique to I61Q hearts (clusters 1 and 3; Fig. 2, D and G, and table S1) and (ii) larger and more elongated focal adhesions identified in cardiac fibroblasts from I61Q transgenics (Fig. 3, H to J). As proof of principle that increased diastolic tension induces cardiac fibroblast proliferation, engineered heart tissues (EHTs) were generated with CON cardiac fibroblasts and neonatal myocytes adenovirally transduced with wild-type or I61Q cTnC and subjected to chronic preload in culture [fig. S4, E and F (49, 50)]. While preload increased the percentage of actively proliferating fibroblasts independent of genotype, I61Q cTnC expression had stronger effects (Fig. 3K). The interaction between I61Q cTnC expression and preload also increased tissue and collagen alignment (Fig. 3L), which more accurately modeled the I61Q transgenic phenotype than unloaded I61Q EHTs (Fig. 2X).

Genetically disabling p38-mediated cardiac fibroblast responsiveness reduces DCM severity.

While several mechanotransduction pathways exist within fibroblasts, including those mediated by focal adhesions, ligand-receptor pair analysis of snRNA-seq data also predicted stronger $\mathsf{TGF}\beta$ signaling via *Tgfβr1* overexpression in I61Q cardiac fibroblasts (fig. S5, A and B). Since the response of I61Q cardiac fibroblasts to TGFB in culture was similar to CON (fig. S3, A and B) other mechanotransduction pathways that could underlie cardiac fibroblast expansion in I61Q mice were examined. YAP, a well-established index of mechanotransduction and regulator of proliferation (51– 53), had higher activity in I61Q cardiac fibroblasts as identified by nuclear translocation assay (fig. S5C). Our previous findings demonstrated that in cardiac fibroblasts both TGFB signaling and strain-dependent increases in YAP-TEAD mechanotransduction require p38 activity (46, 54). In accordance with these findings, p38 activity was increased in cardiac fibroblasts from 2-monthold I61Q transgenics as measured by Western blot and p38 nuclear translocation assays (fig. S5, D to F). Given these data

First release: 11 September 2025

conditional p38 deletion in cardiac fibroblasts (p38 KO) was used to determine if p38 was essential for fibroblast expansion in response to I61Q-cTnC and ultimately the DCM phenotype. So, I61Q cTnC transgenics were crossed with cardiac fibroblast-specific p38 KOs, giving rise to four experimental genotypes (Fig. 4A): controls (CON), p38 KO, I61Q, and I61Q plus fibroblast-specific p38 KO (p38 KO I61Q). All experimental weanlings received one week of TAM by intraperitoneal injection followed by 10 weeks of TAM chow (Fig. 4B), which elicits ~85% recombination efficiency and nearly complete loss of p38 by 2 weeks in Tcf21⁺ fibroblasts (46). snRNA-seg of whole heart nuclei demonstrated that cardiac fibroblast-specific p38 deletion reduced the proportion of fibroblasts that transition to states 1 and 3, which were unique to mice expressing I61Q cTnC and defined by the up-regulation of transcripts involved in cell cycle activity and mechanotransduction (Figs. 2G and 4, C and D; I61Q and CON Uniform Manifold Approximation and Projections (UMAPs) are also shown in Fig. 2D and fig. S5, G to J). p38 deletion also lowered the expression of Col1a1, Col1a2, and Col3a1 (fig. S3, L to N) and restored several myocytefibroblast crosstalk pathways to control levels (fig. S5, A and B). Myocardial sections immunostained with PDGFRα and pHH3 antibodies validated the snRNA-seq findings, as p38 KO-I61Q myocardium had reduced numbers of actively proliferating PDGFR α^+ ,pHH3⁺ fibroblasts when compared to I61Q alone (Fig. 4E). Concomitant with lower cell cycle activity PDGFRα⁺ fibroblast density was reduced in p38 KO-I61Q mice (Fig. 4F). Deeper bioinformatic analysis of cell cycle regulatory signals that were overexpressed in I61Q but down-regulated in p38KO-I61Q fibroblasts identified early growth response gene 1 (Egr1), which is a transcription factor downstream of integrin receptor signaling involved in proliferation, fibrosis, and pro-regeneration fibroblast senescence (55–57). RT-qPCR confirmed Egr1 is up-regulated in 161Q cardiac fibroblasts (fig. S5K). EGR1 was also found in the nuclei of PDGFRα⁺ fibroblasts in I61Q myocardium, but was non-existent in age matched CON and p38 KO-I61Q cardiac sections (Fig. 4G). To determine if *Egr1* is sufficient to induce cardiac fibroblast proliferation, 2-month-old CON and I61Q cardiac fibroblasts were retrovirally transduced with human EGR1 and the percentage of proliferating fibroblasts quantified by EdU positivity (Fig. 4H and fig. S5L). EGR1 overexpression increased CON fibroblast proliferation to the same level as I61Q fibroblasts transduced with dsRed (control), whereas EGR1 overexpression had no additive effects on proliferation in I61Q fibroblasts (Fig. 4H). The addition of a p38 inhibitor (SB203580, 10 µmol/L) reduced proliferation in both CON and I61Q cardiac fibroblasts treated with dsRed virus, but EGR1 overexpression in tandem with p38 inhibition restored proliferation to normal I61Q levels (Fig. 4H). These data demonstrate that Egr1 initiates fibroblast proliferation and acts downstream of p38.

Four-month-old myocardial sections stained with picrosirius red-fast green showed that fibroblast-specific p38 deficiency in

I61Q transgenics (p38 KO-I61Q) blocked interstitial fibrosis at this later timepoint (Fig. 4, I and J, and fig. S5M). Analysis of collagen fiber alignment by SHG imaging of decellularized hearts demonstrated that in most of the p38 KO-I61Q cohort collagen fibers were less aligned and more like controls (Fig. 4K). To confirm that alterations in cardiac fibroblast proliferation and matrix phenotype were due to p38-dependent changes in fibroblast function rather than altered primary sarcomere contractile defects from 161Q cTnC, Ca²⁺-activated force generation was measured in demembranated trabecula from all of the experimental genotypes. As represented by a marked rightward shift in the isometric cardiac muscle force-Ca2+ relationship (Fig. 4L), the I61Q cTnC transgene-dependent decrease in force generation at half-maximal Ca²⁺ concentrations (pCa₅₀) was retained in p38 KO-I61Q cardiac muscle when compared to CON and p38 KO (Fig. 4, L and M), demonstrating fibroblast-specific p38 deficiency fails to correct the desensitization of the myofilaments to Ca²⁺ in I61Q mice. Unexpectedly, intact cardiac muscle from p38 KO-I61Q generated higher twitch forces with improved contractility when compared to I61Q (Fig. 4N and fig. S6, A and B). Functional rescue of the I61Q cTnC phenotype was also observed at the whole heart level by echocardiography in which p38 KO-I61Q mice had a significant recovery in ejection fraction (Fig. 40; P < 0.05). Invasive hemodynamics further confirmed that p38 KO-I61Q mice improved systolic function relative to I61Q transgenics, as cardiac stroke work, ESPVR, and stroke volume were all restored to control levels (Fig. 4, P and Q, and fig. S6, C to E). We've ascribed this restoration of twitch force and pressure development in p38 KO-I61Q hearts to reduced fibroblast numbers that should prevent early myocardial stiffening (Fig. 4, F, I, and J), although Starling effects from the increased preload in p38 KO-I61Q cannot be ruled out as a factor (Fig. 4P). This is in contrast to I61Q mice that operate at much higher end diastolic volume but with reduced stroke volume indicating I61Q hearts are stretched beyond their preload reserve (Fig. 4P and fig. S6D).

To determine how disabling p38 in cardiac fibroblasts could correct myocyte contractile function, single myocyte contraction and Ca²⁺ kinetics were assayed. Unloaded shortening amplitude was reduced in I61Q cardiomyocytes but completely rescued in the p38 KO-I61Q group (Fig. 4R). This rescue was likely driven by increased Ca²⁺ transient amplitudes measured in p38 KO-I61Q cardiomyocytes that were higher relative to all other genotypes (Fig. 4S). To determine if fibroblast-specific p38 deletion also corrected myocardial remodeling of the heart, echocardiography was used to measure diastolic chamber dimensions. Here, p38 KO-I61Q diastolic chamber dimensions were increased at 4 months of age similar to mice expressing just I61Q cTnC (Fig. 4T), which we ascribed to I61Q-dependent reduction in diastolic tone (Fig. 1E) rather than bona fide eccentric hypertrophy from serial sarcomere addition (24). Indeed, assessments of cardiomyocyte morphology in relaxed conditions (+blebbistatin) indicated p38

First release: 11 September 2025

KO-I61Q cardiomyocytes had significantly reduced cell lengths and areas when compared to I61Q (Fig. 4, U and V; P < 0.001). These data collectively demonstrate disabling p38-mediated fibroblast responsiveness to sarcomere hypocontractility alleviates much of the adaptive remodeling and reduces the severity of the DCM phenotype.

Discussion

This study explored the function of fibroblasts as mechanical rheostats within the heart capable of adaptively remodeling the ECM to preserve cardiac function and mechanical homeostasis in response to a DCM-linked sarcomeric variant that causes myocyte hypocontractility. These data suggest fibroblast function is one of a myriad of nested mechanical homeostatic feedback loops guiding organ structure-function in which cells exhibit dynamic reciprocity with their extracellular mechanical environment (58–61). In DCM, fibroblasts are well-equipped to respond to the contractile insufficiencies of cardiomyocytes, as they are necessarily mechanosensitive to fulfill their role of maintaining tissue integrity (62). It is likely that reduced cardiomyocyte tension leads to strain overload as hemodynamic loads on the myocardial wall increase throughout development and disease progression (63). Here, both cardiomyocytes and fibroblasts adapted to the pathogenic cTnC variant to preserve the heart's mechanical integrity and systolic function, where cardiomyocytes altered their morphology and tuned excitation-contraction coupling mechanisms. Both cardiomyocyte adaptations appear to be highly reversible should the inciting disease stimulus be therapeutically blocked or removed. By contrast, cardiac fibroblasts proliferated in response to the I61Q-dependent loss of myocyte tension generation, which is likely a permanent modification given cardiac fibroblasts are resistant to cell death and lack regulatory mechanisms for restricting cell number (64-66). Hence, the tissue alignment, compaction, and stiffness resulting from fibroblast proliferation may also prove irreversible without a fibroblast-specific therapy that blocks their response to sarcomere hypocontractility (46, 54), which was achieved in this study by targeted genetic deletion of p38. This result is supported by a recent report that developmental ablation of cardiac fibroblasts softens myocardial tissue (66). Our finding that the material properties of DCM myocardium are shaped in part by cardiac fibroblast population growth rather than the fibrotic process of fibroblast to myofibroblast transition is critically important to the treatment of non-ischemic DCM (17), given activated myofibroblast states are transient, and unlike changes in fibroblast number, these state transitions could reverse in response to myocyte-specific therapeutics for DCM (64). Promising therapeutic strategies for DCM like myosin activators may not correct fibroblast proliferation, which could explain their modest effects on tissue stiffening (7, 8). It is therefore unlikely that correcting myocyte tension generation alone could reduce fibroblast numbers in the DCM heart unless given at the earliest

stage of the disease process. Lastly, this study challenges the paradigm that ECM remodeling is secondary to eccentric hypertrophy of the myocyte and instead supports an essential role for fibroblasts and the extracellular environment in shaping cardiac form and function in DCM (67), indicating effective therapeutics for this disease will need to address collective cell behaviors rather than singularly restore myocyte function.

Materials and methods

Mice

All animal experiments were approved by the University of Washington Institutional Animal Care and Use Committee. I61Q mice were generated as previously described, by mating to a tetracycline transactivator (tTA) line on the FVB/NJ genetic background (2). The I61Q cTnC transgene is under the control of an α -myosin heavy chain promoter which has a small window of expression from day 8-10 post coitum, shuts off, and then is robustly expressed in the ventricle and atria starting at postnatal day 2 through the lifetime of the animal (1, 68). These I61Q tTA mice were further bred onto a line containing LoxP-targeted Mapk14 (p38^{fl/fl}) mice and a tamoxifen regulated Cre recombinase that was knocked into the Tcf21 locus (Tcf21iCre) to generate I61Q cTnC-p38^{fl/fl}-Tcf21^{iCre} mice (p38 l61Q), which were on mixed genetic background (46). This cross yielded the following experimental groups (Fig. 4A): control (CON, genotypes: p38fl/fl-tTA or Tcf21iCre-tTA), fibroblast-specific p38 KO (genotypes: p38fl/fl-Tcf21iCre or p38fl/fl-Tcf21iCre-tTA), I61Q (genotypes: I61Q cTnC-tTAp38^{fl/fl} or I61Q cTnC-Tcf21^{iCre}-tTA), and I61Q cTnC with fibroblastspecific p38 KO (genotypes: I61Q-tTA-p38fl/fl-Tcf21iCre). For experimental groups that contain 2 different genotypes, t tests were performed to determine whether they were statistically different. Tamoxifen (TAM) was administered to mice by intraperitoneal injection for 5 consecutive days (400 mg/kg body weight in peanut oil), followed by tamoxifen citrate chow ad libitum until a 2 or 4 month experimental endpoint (Fig. 4B). This tamoxifen dosing regimen elicits ~85% recombination efficiency and ensures that we are maximally recombining all resident cardiac fibroblasts throughout the course of the study, as proliferation of any nonrecombined Tcf21 fibroblast could reduce the effect size. Echocardiography was performed on a Vevo2100 or Vevo3100 under inhalation isoflurane at heart rates exceeding 350 beats per minute (bpm). Invasive hemodynamics on isoflurane-anesthetized mice was performed under heart rates of 420-500 bpm using a high-fidelity pressure-volume catheter (1.2F, Transonic) inserted into the left ventricle via the right carotid artery. All mouse studies are performed with cohorts from multiple inbred pairs with randomized interventions and littermates as controls. To avoid bias, genotypes and experimental groups remain blinded until data are analyzed. Biological replicates are equally comprised of animals/cells from both sexes.

First release: 11 September 2025

Histology

Fixed cardiac tissues were either processed into paraffin and sectioned or cryosectioned in optimum cutting temperature (OCT) compound for histologic assessment. Picrosirius red-fast green stained slides were imaged across 6 fields of view at 20x magnification per heart and segmented for collagen content using the color thresholding tool in ImageJ. Whole-heart cross-section images were generated from slide scans obtained by a Hamamatsu NanoZoomer digital pathology system. For fibroblast proliferation and activation, slides were stained with antibodies for αSMA (Sigma A2547, 1:500), phospho-histone H3 (abcam, 1:200), and PDGFRα (1:100 abcam) overnight in staining buffer (1X PBS, 1% BSA, 1% fish skin gelatin), then stained using Alexa Fluor-conjugated secondaries (1:1000 Thermo Fisher) and Hoechst (1:2000 Thermo Fisher) for 90 min in staining buffer at room temperature. Stained slides were imaged on a Leica Stellaris 5 confocal microscope under 20x magnification. For quantification, images from six representative regions of interest were obtained at 2x scanner zoom and counted manually blinded to mouse genotype using FIJI (55).

Cardiac Perfusion Decellularization

Freshly harvested hearts were retrograde perfused with a 1% sodium dodecyl sulfate (SDS) solution for 12 hours to decellularize, followed by 1% Triton-X 100 for 1 hour to remove SDS, then rinsed by perfusion with deionized water for 1 hour. Hearts were then transferred to 15 mL deionized water, which was refreshed daily for 5 days to ensure complete removal of detergent.

Multiphoton ECM imaging and structural analysis

Hearts were perfused with 1% agarose and mounted on a 100 mm petri dish with the left ventricular free wall facing up, then imaged in whole mount on an Olympus FV1000MP microscope using 860 nm excitation from a Mai-Tai HP laser (Spectra Physics, 59% power) and a Violet/Green emission filter cube. Z-stacks consisting of 20 images with 1.5-micron step within the left ventricular free wall starting 10 micron below the epicardial surface were condensed into maximum intensity projections using ImageJ, then the SHG channel (violet) was quantified for fiber alignment and length using CurveAlign 4.0 beta in CT-FIRE fiber mode (69, 70).

Transmission Electron Microscopy (TEM)

To examine changes in individual collagen fiber architecture, hearts from CON and I61Q mice were excised and 2 mm tissue cubes were cut out of the myocardium and prepped for electron microscopy. Samples were immediately fixed in 4% Glutaraldehyde in 0.1M sodium cacodylate buffer, then stored overnight at 4C. The tissues were washed 5×5 min in buffer at room temperature and post fixed in buffered 2% osmium tetroxide on ice for 1 hour. The tissues were subsequently washed 5 times in ddH20,

then en bloc stained in 1% uranyl acetate (aqueous) overnight at 4C. The next day the tissue was washed for 5 min in ddH2O then dehydrated in ice cold 30%, 50%, 70%, and 95% ETOH. Samples were then allowed to come to room temperature. This was followed by 2 changes of 100% ETOH and two changes of propylene oxide. The tissue was then infiltrated in a 1:1 mixture of propylene oxide: Epon Araldite resin, for 2 hours followed by two changes of fresh Epon Araldite, 2 hours each change, then placed in flat embedding molds and polymerized at 60°C overnight. Thin sections of 80 nm were cut on a Leica EM UC7, post stained with Reynolds Lead Citrate, and imaged on a JEOL 1230 at 80KV. Individual fibrils were segmented using Cellpose-SAM (71) and fibril density, diameter, and cross-sectional area was quantified using FIJI. Analysis was performed on 20 images from each genotype.

Cardiac muscle and ECM mechanics

For passive mechanics studies, a Langendorff balloon was inserted into the left ventricle and the heart was perfused with Krebs-Henseleit buffer containing blebbistatin (25 μM , Toronto Research Chemicals). The balloon was inflated in 5 μL steps to 35 μL with 2 min of stress relaxation time between each step. This regimen was performed once to precondition the tissue, and then repeated in duplicate for measurements of developed pressure. Following passive muscle measurements, the heart was decellularized as above, with the balloon remaining inserted in the left ventricle, and the mechanical testing regimen was repeated for the ECM alone. Pressure traces were acquired using LabView and exported to Excel for analysis of developed pressure and curve slope.

ECM Proteomics

First release: 11 September 2025

Hearts were perfusion decellularized as described above, and digested in solution as previously described (58). Samples were first denatured for 2 hours at 37°C in urea (8 M, Fisher) and dithiothreitol (10 mM, Thermo Fisher) under continuous agitation. Following 30 min of alkylation with iodoacetamide (25 mM, supplier), samples were then diluted with ammonium bicarbonate (100 mM, pH=8.0, Sigma Aldrich), and 2 µL PNGase F (500 U/μL, New England Biolabs) was added to deglycosylate the samples over a 2 hour incubation at 37°C. Samples were then digested by adding 2 μL LysC (500 ng/μL, Pierce) for 2 hours, then 6 μL trypsin (100 ng/μL, New England Biolabs) overnight, both at 37°C. Trypsin (4 µL) was added the next day for 2 hours of additional digestion at 37°C, then inactivated through addition of 50% trifluoracetic acid (Sigma Aldrich) before samples were clarified through centrifugation (16,000 × g, 5 min) and cleaned for liquid chromatography on an MCX column (Waters). For proteomics by data independent acquisition (DIA) mass spectrometry, samples were analyzed on a Q Exactive HF Hybrid Quadrupole-Orbitrap Mass Spectrometer (Thermo Fisher) with a Nanoacquity HPLC (Waters). Total ion currents were normalized between samples

using the PowerTransformer function of the scikit-learn package in Python, then differential expression between groups was tested by one-way analysis of variance (ANOVA) (59). Figures were generated using Seaborn and matplotlib (60).

Cardiac fibroblast isolation and culture

Primary cardiac fibroblasts were isolated as described previously (30). Fibroblasts for RT-PCR and Western blot analyses were negatively sorted on Cd11b microbeads and positively sorted for antifeeder microbeads through LS columns on a QuadroMACS magnet (Miltenyi Biotec). Fibroblasts for RNASeq, proliferation assays, and engineered tissues were plated on 60 mm tissue culture dishes and expanded to the first passage in Dulbecco's Modified Eagle Medium (DMEM) with 20% fetal bovine serum (FBS) and 1X penicillin/streptomycin solution. Cells in culture were passaged with 0.25% trypsin-EDTA and seeded onto 24-well iBidi μ-plates at a density of 1000 cells/cm² for in vitro proliferation studies. The FBS concentration in the media was dropped to 2% upon seeding, and EdU (10 μM, Thermo Fisher), dinaciclib (5 μM, ApexBio), or ilomastat (10 μM, MedChemExpress) were added where indicated. After 24 hours, cells were fixed in 4% paraformaldehyde and stained using a Click-It EdU proliferation kit (Thermo Fisher) per manufacturer's instructions. To screen ECM components, 250,000 control cardiac fibroblasts were seeded onto an ECM Select Array Kit Ultra-36 (Advanced Biomatrix) and cultured for 24 hours in EdU-containing media as above. Collagen gel compaction was assayed as previously described (29, 61), with fibroblasts seeded into 1% collagen type I (Advanced Biomatrix) hydrogels at a density of 80,000 cells/mL in a 24-well plate for 24 hours in DMEM with 2% FBS.

PEG-ECM hydrogels

4-armed PEG_{20kDa}-BCN, NHS-Azide, and the MMP-degradable crosslinking peptide N₃-RGPQGIWGQLPETGGRK(N₃)-NH₂ were all synthesized as previously described (37, 62). To generate soluble ECM peptides, 4 hearts per genotype were pooled, snap frozen and homogenized by mortar and pestle under liquid nitrogen, lyophilized to a powder, then resuspended at 10 mg/mL in a pepsin solution (1 mg/mL in 0.1 M hydrochloric acid) for 48 hours at room temperature, and stirred. Digested ECM was neutralized with the addition of NaOH and re-lyophilized. Digested ECM was resuspended at 25 mg/mL in PBS. To azide-functionalize ECM, 2 μL of NHS-Azide (60 mM in DMSO) was added to 118 μL of ECM solution and reacted for 1 hour on ice. Primary cardiac fibroblasts were encapsulated at 10 million cells/mL in gels composed of 3 mM PEG-BCN, 6 mM crosslink, 1 mM N₃-GRGDS, and 5 mg/mL azide-modified ECM, which were then cultured in DMEM containing 10% FBS and 10 µM EdU for 24 hours prior to fixation. Gels were then blocked in PBS containing 0.1M sodium azide to quench any remaining BCN groups in the polymer network and stained as above.

Bulk RNA Sequencing and Analysis

Fibroblasts cultured to 80% confluency were lysed in Trizol (Thermo Fisher), and total RNA was extracted using a Direct-zol RNA Microprep kit, including DNAse treatment (Zymo Research). For RNAseq, RNA integrity was verified using RNA Screentape on a 2200 Tapestation (Agilent) and samples with high RNA integrity (RINe ≥ 7) were submitted to BGI Genomics for RNA sequencing (PE100). Resultant FASTQ files were aligned to the mm10 reference genome using RNA-STAR (72), assigned to genes using featurecounts (73), and gene transcript counts tested for differential expression using DESeq2 (74). Differentially expressed genes were tested for pathway enrichment using G:Profiler (75), and heatmaps were generated in python using the Seaborn package. RT-PCR was performed as previously described using the Superscript III First-Strand Synthesis System (Thermo Fisher), iTag universal SYBR Green Supermix (Bio-Rad), and the primers listed in table S2 (44).

snRNA-seq of whole hearts

First release: 11 September 2025

Whole heart samples were prepared using the sci-RNA-seq3 combinatorial indexing method as described previously with the following modifications (76, 77). Two hearts from each group were snap frozen in liquid nitrogen. Nuclei were isolated from frozen tissues by grinding the frozen tissue with a mortar and pestle, lysing the powdered tissue in hypotonic lysis buffer B, and dissociating the tissue in a gentleMACS M tube run on the "Protein 001" program followed by 50 strokes in a Dounce homogenizer with a type A/loose pestle. Lysates were subsequently filtered through a 40 µm filter and centrifuged at 500xg for 5 min at 4°C. The nuclear pellet was then resuspended in 0.3 M sucrose, phosphate buffered saline (PBS), Triton X-100 MgCl₂ (SPBSTM) buffer (76, 77), which was filtered through a 20µm filter. The nuclei were subsequently fixed in methanol/DSP for 5 min at room temperature. Fixed nuclei were rehydrated with 0.3 M SPBSTM, centrifuged at 500xg for 5 min at 4°C, and resuspended in 0.3 M SPBSTM. Sequencing was performed at the Northwest Genomics Center on a Novaseq 6000 flow cell. Cleaned reads were aligned to the reference genome (GRCm38/mm10) using STAR (72). Doublets were identified using scrublet and subsequently filtered out (78). Further analysis and quality filtering was performed using the Seurat package in R (79). Nuclei were filtered out if they contained fewer than 200 UMI, over the top 1% quantile of UMI, or over 5% mitochondrial reads. Overall, 41,014 singlets across all cell types were sequenced with a mean UMI of 687. Clustering was then performed following the standard approach, with cell types manually identified by canonical marker genes. For fibroblast subcluster analysis, fibroblast reads were then normalized using the SCTransform function with the "glmGamPoi" method. Mitochondrial mapping rate was regressed out using the vars.to.regress argument. Principal component analysis was performed on the

scaled data, and then cells were clustered on the first 5 principal components using the FindNeighbors function and the FindClusters function with resolution 0.3. To visualize the data, non-linear dimensional reduction via UMAP was used to project cells in 2D space on the basis of the first 5 principal components. 5 fibroblast clusters were identified and cluster markers were identified using FindAllMarkers. The data have been deposited at Gene Expression Omnibus (GEO) repository and have been assigned the GEO accession number: GSE294563. GSM8911388-GSM8911399 were the accession numbers assigned to each of the individual data files.

For ligand-receptor pair analysis the ICELLNET package was used following the standard workflow described in the package vignette (80). To ensure cell-type specificity in the communication analysis, each cell type within a pair was specifically subsetted based on identity from the larger global Seurat object and combined into a new object containing only the 2 specified cell types for analysis. The ICELLNET analysis was subsequently performed to identify outgoing and incoming signals with respect to the fibroblasts between fibroblast-cardiomyocyte, fibroblast-endothelial, fibroblast-immune cell, and fibroblast-fibroblast intercellular communication networks. The intercellular interaction scores generated by the ICELLNET analysis were subsequently normalized to wild-type values and averaged by genotype for plotting. The process was repeated for each cell type pairing.

Western blotting

Magnetically sorted fibroblast pellets were lysed in 120 µL of Laemmli Buffer with DTT, of which 30 μL was loaded onto a 10% acrylamide gel for SDS-polyacrylamide gel electrophoresis (SDS-PAGE) and wet transfer to a polyvinylidene fluoride membrane for immunodetection. Membranes were blocked and immunostained in tris-buffered saline (20 mM Tris, 150 mM NaCl, pH 7.6) containing 0.1% Tween 20 and 5% nonfat powdered milk. Primary antibodies for phospho-p38 MAPK (Cell Signaling 9211, 1:1000), total p38 MAPK (Cell Signaling 9212, 1:1000), and GAPDH (Fitzgerald 10R-2932, 1:10,000) were incubated overnight at 4°C under gentle agitation. Rabbit or mouse primary antibodies were detected using a horseradish peroxidase-conjugated anti-rabbit IgG (Sigma AP307P, 1:4000) or anti-mouse IgG (Sigma AP308P, 1:4000) secondary antibody for 90 min at room temperature, then developed using SuperSignal West Pico PLUS (Thermo Fisher) chemiluminescence substrate. The titin N2B isoform was expressed relative to the total titin, meaning the sum of the isoforms N2B and N2BA. This was measured on a Coomassiestained titin gel. For the phosphospecific antibodies, the titin signal on the Western blot was normalized to the corresponding signal on the Coomassie-stained stained blotting membrane, to account for differences in loading. The antibodies and protocols used were derived in the Linke lab (26). The list of antibodies is in Table S3.

Mouse cardiomyocyte isolation and cell culture

For functional measurements, mouse ventricular cardiomyocytes were freshly isolated by Langendorff perfusion with Liberase TM (0.225 mg/mL, Roche) in Krebs-Henseleit buffer (135 mM NaCl, 4.7 mM KCl, 0.6 mM KH₂PO₄, 0.6 mM Na₂HPO₄, 1.2 mM MgSO₄, 20 mM HEPES, 10 µM BDM, and 30 mM taurine) as previously described (81). Ventricular cardiomyocytes were mechanically dispersed and filtered through a 200 µm nylon mesh then allowed to sediment for 5-10 min. Sedimentation was repeated three times using increasing [Ca²⁺] from 0.125 to 0.25 to 0.5 mmol/L. Cardiomyocytes were plated on laminin-coated coverslips in Tyrode's solution (137 mM NaCl, 5.4 mM KCl, 0.5 mM MgCl₂, 1.2 mM CaCl₂•2H₂O, 10 mM HEPES, and 5 mM Glucose, pH 7.4) for 1 hour at 37°C prior to functional measurements. For myocyte morphology measurements, cardiomyocytes were similarly isolated and plated with buffers containing 25 µM blebbistatin and subsequently fixed with 4% PFA at room temperature for 15 min.

Measurements of cardiomyocyte contractility and calcium transients

Sarcomere measurements were obtained from isolated cardiomyocytes using the IonOptix SarcLen Sarcomere Length Acquisition Module with a MyoCam-S3 digital camera (Ionoptix Co.) attached to an Olympus uWD 40 inverted microscope. For these measurements, cardiomyocytes were bathed in 1.2 mM Ca²⁺ Tyrode's solution and kept at 37°C. To jumpstart pacing, cardiomyocytes were stimulated with frequencies varying from 0.5, 1.0, and 1.5 Hz at 10 V for a minimum of 10 contractions at each frequency. Sarcomere lengths were then measured in real time at a frequency of 1 Hz and averaged across 10-15 contraction cycles. Separate coverslips were treated with 1 µM Fura-2-acetoxymethyl ester to measure calcium transients. Blinded analysis was performed using the IonWizard software. Statistical analyses were performed on individual myocyte measurements (n \sim 20 cardiomyocytes/mouse; n=3-4). Significance was determined using Student's t test. For myocyte geometry quantification, approximately 50 cells per mouse were manually traced using FIJI.

Rat cardiomyocyte isolation and EHT experiments

First release: 11 September 2025

Freshly isolated neonatal rat cardiomyocytes and fibroblasts were seeded into 100 µL fibrin EHTs containing 1 million cells per tissue between a pair of flexible and rigid PDMS posts that were 12 mm in length and 1.5 mm in diameter within a 24-well plate, as previously described (82). EHTs were polymerized for 85 min, then demolded and immersed in plating media [4:1 DMEM:Medium 199 (M199), 10% horse serum, 5% FBS, 100 U/mL penicillin streptomycin (pen-strep)] containing AdGFP or AdI61Q at a multiplicity of infection of 200. After 24 hours, EHTs were switched to maintenance medium consisting of 1:1 DMEM:M199 containing 5% FBS, 100 U/mL pen-strep, 5 g/L 6-aminocaproic acid, 1X insulin-transferrin-selenium, and 0.1% chemically defined lipid concentrate,

which was thenceforth swapped every other day until the 14-day experimental endpoint. EHTs were then bathed in Tyrode's buffer equilibrated to 37°C for contractile analysis as previously described (82). Briefly, EHTs were paced at 1 Hz by a custom 24-well plate pacing apparatus with carbon electrodes biphasically stimulated (5V/cm, 10ms duration) with a medical stimulator (Astro Med Grass Stimulator, Model S88X) while imaged. Brightfield videos of PDMS post deflection during EHT contraction were taken at 66.67 frames per second on a Nikon TEi epi-fluorescent microscope. Deflection of the flexible post relative to the rigid post was tracked using a custom MATLAB script in order to calculate passive force, twitch force, and the area under the twitch curve (tension index). Following functional measurements, EHTs were fixed in ice-cold 4% PFA for 1 hour and stained with anti-FLAG (Sigma, 1:1000), Alexa Fluor 568-conjugated wheat germ agglutinin (Thermo Fisher 1:1000), and Hoechst 33342 (Thermo Fisher, 1:1000). For alignment, 8 ROIs per wheat-germ stained EHT were confocally imaged in whole mount on a Leica Stellaris 5 confocal microscope and analyzed using the Directionality plugin in FIJI. Alignment coefficient was calculated as the amount divided by the dispersion of directionality.

Intact and skinned muscle mechanics

Hearts were quickly removed via thoracotomy and rinsed in oxygenated modified Krebs buffer containing 118.5 mM NaCl, 5 mM KCl, 1.2 mM MgSO₄, 2 mM NaH₂PO₄, 25 mM NaHCO₃, 1.8 mM CaCl₂, and 10 mM glucose. Hearts were then perfused and dissected in oxygenated modified Krebs with 0.1 mM CaCl₂ and 20 mM 2,3-butanedione 2-monoxime (BDM) to limit contraction and damage during tissue dissection.

For demembranated tissue mechanics, dissected hearts were permeabilized in a glycerol relaxing solution containing 100 mM KCl, 10 mM MOPS, 5 mM K₂EGTA, 9 mM MgCl₂ and 5 mM Na₂ATP (pH 7.0), 1% (by vol) Triton X-100, 1% protease inhibitor (Sigma P8340), and 50% (by vol) glycerol at 4°C overnight then stored in Read and the second of the second o tracked using a custom MATLAB script in order to calculate pas-

P8340), and 50% (by vol) glycerol at 4°C overnight then stored in fresh solution without Triton X-100 for storage at -20°C. Briefly, right ventricular trabeculae were dissected and mounted between a force transducer and motor, and sarcomere length (SL) was set to ~2.3 μm, as previously described (5). Experiments were conducted in a physiological solution (15°C, pH 7.0) containing a range of pCa (= $-\log[Ca^{2+}]$) from 9.0 to 4.0. Force and k_{tr} (rate of tension redevelopment) were collected at each pCa and analyzed with custom using LabView software.

For intact twitch measurements unbranched, intact trabeculae were dissected from the right ventricular wall and mounted between a force transducer (Cambridge Technology, Inc., model 400A) and a rigid post, as previously described (5). The tissue was then submerged in a custom experimental chamber that was continuously perfused with oxygenated modified Krebs buffer (1.8 mM CaCl₂) at 33°C. After a ~20 min equilibration and washout at 0.5 Hz pacing, optimal length was set to ~2.3 µm SL and tissue was

paced at 1 Hz. 30 s traces were recorded on custom LabView software and were analyzed with custom code written using MATLAB software (Mathworks).

REFERENCES AND NOTES

- 1. J. Davis, L. C. Davis, R. N. Correll, C. A. Makarewich, J. A. Schwanekamp, F. Moussavi-Harami, D. Wang, A. J. York, H. Wu, S. R. Houser, C. E. Seidman, J. G. Seidman, M. Regnier, J. M. Metzger, J. C. Wu, J. D. Molkentin, A Tension-Based Model Distinguishes Hypertrophic versus Dilated Cardiomyopathy. Cell 165, 1147-1159 (2016). doi:10.1016/j.cell.2016.04.002 Medline
- 2. J. D. Powers, K. B. Kooiker, A. B. Mason, A. E. Teitgen, G. V. Flint, J. C. Tardiff, S. D. Schwartz, A. D. McCulloch, M. Regnier, J. Davis, F. Moussavi-Harami, Modulating the tension-time integral of the cardiac twitch prevents dilated cardiomyopathy in murine hearts. JCI Insight 5, e142446 (2020). doi:10.1172/jci.insight.142446 Medline
- 3. R. Yotti, C. E. Seidman, J. G. Seidman, Advances in the Genetic Basis and Pathogenesis of Sarcomere Cardiomyopathies. Annu. Rev. Genomics Hum. Genet. 20, 129-153 (2019). doi:10.1146/annurev-genom-083118-015306 Medline
- 4. G. W. Dec, V. Fuster, Idiopathic dilated cardiomyopathy. N. Engl. J. Med. 331, 1564-1575 (1994). doi:10.1056/NEJM199412083312307 Medline
- 5. R. E. Hershberger, D. J. Hedges, A. Morales, Dilated cardiomyopathy: The complexity of a diverse genetic architecture. Nat. Rev. Cardiol. 10, 531-547 (2013). doi:10.1038/nrcardio.2013.105 Medline
- 6. E. M. McNally, J. R. Golbus, M. J. Puckelwartz, Genetic mutations and mechanisms in dilated cardiomyopathy. J. Clin. Invest. 123, 19-26 (2013). doi:10.1172/JCI62862 Medline
- 7. J. R. Teerlink, R. Diaz, G. M. Felker, J. J. V. McMurray, M. Metra, S. D. Solomon, K. F. Adams, I. Anand, A. Arias-Mendoza, T. Biering-Sørensen, M. Böhm, D. Bonderman, J. G. F. Cleland, R. Corbalan, M. G. Crespo-Leiro, U. Dahlström, L. E. Echeverria, J. C. Fang, G. Filippatos, C. Fonseca, E. Goncalvesova, A. R. Goudey, J. G. Howlett, D. E. Lanfear, J. Li, M. Lund, P. Macdonald, V. Mareev, S. I. Momomura, E. O'Meara, A. Parkhomenko, P. Ponikowski, F. J. A. Ramires, P. Serpytis, K. Sliwa, J. Spinar, T. M. Suter, J. Tomcsanyi, H. Vandekerckhove, D. Vinereanu, A. A. Voors, M. B. Yilmaz, F. Zannad, L. Sharpsten, J. C. Legg, C. Varin, N. Honarpour, S. A. Abbasi, F. I. Malik, C. E. Kurtz; GALACTIC-HF Investigators, Cardiac Myosin Activation with Omecamtiv Mecarbil in Systolic 384, Failure. N. Engl. J. Med. 105-116 doi:10.1056/NEJMoa2025797 Medline
- 8. S. Saberi, N. Cardim, M. Yamani, J. Schulz-Menger, W. Li, V. Florea, A. J. Sehnert, R. Y. Kwong, M. Jerosch-Herold, A. Masri, A. Owens, N. K. Lakdawala, C. M. Kramer, M. Sherrid, T. Seidler, A. Wang, F. Sedaghat-Hamedani, B. Meder, O. Havakuk, D. Jacoby, Mavacamten Favorably Impacts Cardiac Structure in Obstructive Hypertrophic Cardiomyopathy: EXPLORER-HCM Cardiac Magnetic Resonance Substudy Analysis. Circulation 143, 606–608 (2021). doi:10.1161/CIRCULATIONAHA.120.052359 Medline
- 9. A. E. Deranek, M. M. Klass, J. C. Tardiff, Moving beyond simple answers to complex disorders in sarcomeric cardiomyopathies: The role of integrated systems. Pflugers Arch. 471, 661-671 (2019). doi:10.1007/s00424-019-02269-0 Medline
- 10. A. Gulati, A. G. Japp, S. Raza, B. P. Halliday, D. A. Jones, S. Newsome, N. A. Ismail, K. Morarji, J. Khwaja, N. Spath, C. Shakespeare, P. R. Kalra, G. Lloyd, A. Mathur, J. G. F. Cleland, M. R. Cowie, R. G. Assomull, D. J. Pennell, T. F. Ismail, S. K. Prasad, Absence of Myocardial Fibrosis Predicts Favorable Long-Term Survival in New-Onset Heart Failure. Circ. Cardiovasc. Imaging 11, e007722 (2018). doi:10.1161/CIRCIMAGING.118.007722 Medline
- 11. B. P. Halliday, A. J. Baksi, A. Gulati, A. Ali, S. Newsome, C. Izgi, M. Arzanauskaite, A. Lota, U. Taval, V. S. Vassiliou, J. Gregson, F. Alpendurada, M. P. Frenneaux, S. A. Cook, J. G. F. Cleland, D. J. Pennell, S. K. Prasad, Outcome in Dilated Cardiomyopathy Related to the Extent, Location, and Pattern of Late Gadolinium Enhancement. JACC Cardiovasc. Imaging 12, 1645–1655 (2019). doi:10.1016/j.jcmg.2018.07.015 Medline
- 12. A. Mandawat, P. Chattranukulchai, A. Mandawat, A. J. Blood, S. Ambati, B. Hayes, W. Rehwald, H. W. Kim, J. F. Heitner, D. J. Shah, I. Klem, Progression of

First release: 11 September 2025

- Myocardial Fibrosis in Nonischemic DCM and Association With Mortality and Heart Failure Outcomes. JACC Cardiovasc. Imaging 14, 1338-1350 (2021). doi:10.1016/j.jcmg.2020.11.006 Medline
- 13. A. Acharya, S. T. Baek, G. Huang, B. Eskiocak, S. Goetsch, C. Y. Sung, S. Banfi, M. F. Sauer, G. S. Olsen, J. S. Duffield, E. N. Olson, M. D. Tallquist, The bHLH transcription factor Tcf21 is required for lineage-specific EMT of cardiac fibroblast progenitors. Development 139, 2139-2149 (2012). doi:10.1242/dev.079970 Medline
- 14. S. R. Ali, S. Ranjbarvaziri, M. Talkhabi, P. Zhao, A. Subat, A. Hojjat, P. Kamran, A. M. S. Müller, K. S. Volz, Z. Tang, K. Red-Horse, R. Ardehali, Developmental heterogeneity of cardiac fibroblasts does not predict pathological proliferation activation. Circ. Res. 625-635 (2014).doi:10.1161/CIRCRESAHA.115.303794 Medline
- 15. O. Kanisicak, H. Khalil, M. J. Ivey, J. Karch, B. D. Maliken, R. N. Correll, M. J. Brody, S. C. J Lin, B. J. Aronow, M. D. Tallquist, J. D. Molkentin, Genetic lineage tracing defines myofibroblast origin and function in the injured heart. Nat. Commun. 7, 12260 (2016). doi:10.1038/ncomms12260 Medline
- 16. T. Moore-Morris, N. Guimarães-Camboa, I. Banerjee, A. C. Zambon, T. Kisseleva, A. Velayoudon, W. B. Stallcup, Y. Gu, N. D. Dalton, M. Cedenilla, R. Gomez-Amaro, B. Zhou, D. A. Brenner, K. L. Peterson, J. Chen, S. M. Evans, Resident fibroblast lineages mediate pressure overload-induced cardiac fibrosis. J. Clin. Invest. 124, 2921–2934 (2014). doi:10.1172/JCI74783 Medline
- 17. R. Bretherton, D. Bugg, E. Olszewski, J. Davis, Regulators of cardiac fibroblast 117-135 (2020). state. Matrix Biol. 91-92. doi:10.1016/j.matbio.2020.04.002 Medline
- 18. J. D. Humphrey, E. R. Dufresne, M. A. Schwartz, Mechanotransduction and extracellular matrix homeostasis. Nat. Rev. Mol. Cell Biol. 15, 802-812 (2014). doi:10.1038/nrm3896 Medline
- 19. J. J. Saucerman, P. M. Tan, K. S. Buchholz, A. D. McCulloch, J. H. Omens, Mechanical regulation of gene expression in cardiac myocytes and fibroblasts. Nat. Rev. Cardiol. 16, 361-378 (2019). doi:10.1038/s41569-019-0155-8 Medline
- 20. K. L. Kreutziger, N. Piroddi, J. T. McMichael, C. Tesi, C. Poggesi, M. Regnier, Calcium binding kinetics of troponin C strongly modulate cooperative activation and tension kinetics in cardiac muscle. J. Mol. Cell. Cardiol. 50, 165-174 (2011). doi:10.1016/j.yjmcc.2010.10.025 Medline
- 21. S. B. Tikunova, J. P. Davis, Designing calcium-sensitizing mutations in the regulatory domain of cardiac troponin C. J. Biol. Chem. 279, 35341-35352 (2004). doi:10.1074/jbc.M405413200 Medline
- 22. S. M. Haldar, D. Srivastava, Sarcomeres and Cardiac Growth: Tension in the Relationship. Trends Mol. 22, 530-533 Med. doi:10.1016/j.molmed.2016.05.001 Medline
- 23. I. Kehat, J. D. Molkentin, Molecular pathways underlying cardiac remodeling during pathophysiological stimulation. Circulation 122, 2727-2735 (2010). doi:10.1161/CIRCULATIONAHA.110.942268 Medline
- 24. I. Kehat, J. Davis, M. Tiburcy, F. Accornero, M. K. Saba-El-Leil, M. Maillet, A. J. York, J. N. Lorenz, W. H. Zimmermann, S. Meloche, J. D. Molkentin, Extracellular signal-regulated kinases 1 and 2 regulate the balance between eccentric and concentric cardiac growth. Circ. Res. 108, 176-183 (2011). doi:10.1161/CIRCRESAHA.110.231514 Medline
- 25. C. S. Chung, H. L. Granzier, Contribution of titin and extracellular matrix to passive pressure and measurement of sarcomere length in the mouse left 731-739 Cell. Cardiol. 50. (2011). ventricle. I. Mol. doi:10.1016/j.yjmcc.2011.01.005 Medline
- 26. N. Hamdani, M. Herwig, W. A. Linke, Tampering with springs: Phosphorylation of titin affecting the mechanical function of cardiomyocytes. Biophys. Rev. 9, 225–237 (2017). doi:10.1007/s12551-017-0263-9 Medline
- 27. M. M. LeWinter, H. L. Granzier, Cardiac titin and heart disease. J. Cardiovasc. Pharmacol. 63, 207-212 (2014). doi:10.1097/FJC.00000000000000 Medline
- 28. R. O. Hynes, A. Naba, Overview of the matrisome—An inventory of extracellular matrix constituents and functions. Cold Spring Harb. Perspect. Biol. 4, a004903 (2012). doi:10.1101/cshperspect.a004903 Medline
- 29. M. Cescon, F. Gattazzo, P. Chen, P. Bonaldo, Collagen VI at a glance. J. Cell Sci. 128, 3525-3531 (2015). Medline

- 30. J. A. Chirinos, L. Zhao, A. L. Reese-Petersen, J. B. Cohen, F. Genovese, A. M. Richards, R. N. Doughty, J. Díez, A. González, R. Querejeta, P. Zamani, J. Nuñez, Z. Wang, C. Ebert, K. Kammerhoff, J. Maranville, M. Basso, C. Qian, D. G. K. Rasmussen, P. H. Schafer, D. SeifFert, M. A. Karsdal, D. A. Gordon, F. Ramirez-Valle, T. P. Cappola, Endotrophin, a Collagen VI Formation-Derived Peptide, in Heart Failure. NEJM Evid. 1, 10 (2022). doi:10.1056/EVIDoa2200091 Medline
- 31. K. L. Herrmann, A. D. McCulloch, J. H. Omens, Glycated collagen cross-linking alters cardiac mechanics in volume-overload hypertrophy. Am. J. Physiol. Circ. Physiol. 284, H1277-H1284 (2003).doi:10.1152/ajpheart.00168.2002 Medline
- 32. S. Bansode, U. Bashtanova, R. Li, J. Clark, K. H. Müller, A. Puszkarska, I. Goldberga, H. H. Chetwood, D. G. Reid, L. J. Colwell, J. N. Skepper, C. M. Shanahan, G. Schitter, P. Mesquida, M. J. Duer, Glycation changes molecular organization and charge distribution in type I collagen fibrils. Sci. Rep. 10, 3397 (2020). doi:10.1038/s41598-020-60250-9 Medline
- 33. R. Borst, L. Meyaard, M. I. Pascoal Ramos, Understanding the matrix: Collagen modifications in tumors and their implications for immunotherapy. J. Transl. Med. 22, 382 (2024). doi:10.1186/s12967-024-05199-3 Medline
- 34. P. Fratzl, Collagen: Structure and Mechanics, P. Fratzl, Ed. (Springer US, 2008), pp. 1-13.
- 35. G. M. Fomovsky, S. Thomopoulos, J. W. Holmes, Contribution of extracellular matrix to the mechanical properties of the heart. J. Mol. Cell. Cardiol. 48, 490-496 (2010). doi:10.1016/j.yjmcc.2009.08.003 Medline
- 36. R. P. Wohlgemuth, S. Sriram, K. E. Henricson, D. T. Dinh, S. E. Brashear, L. R. Smith, Strain-dependent dynamic re-alignment of collagen fibers in skeletal muscle extracellular matrix. Acta Biomater. 187, 227-241 (2024). doi:10.1016/j.actbio.2024.08.035 Medline
- 37. B. A. Roeder, K. Kokini, J. E. Sturgis, J. P. Robinson, S. L. Voytik-Harbin, Tensile mechanical properties of three-dimensional type I collagen extracellular matrices with varied microstructure. J. Biomech. Eng. 124, 214-222 (2002). doi:10.1115/1.1449904 Medline
- 38. C. B. Raub, V. Suresh, T. Krasieva, J. Lyubovitsky, J. D. Mih, A. J. Putnam, B. J. Tromberg, S. C. George, Noninvasive assessment of collagen gel microstructure and mechanics using multiphoton microscopy. Biophys. J. 92, 2212-2222 (2007). doi:10.1529/biophysj.106.097998 Medline
- 39. Y. Izu, H. L. Ansorge, G. Zhang, L. J. Soslowsky, P. Bonaldo, M.-L. Chu, D. E. Birk, Dysfunctional tendon collagen fibrillogenesis in collagen VI null mice. Matrix Biol. 30, 53-61 (2011). doi:10.1016/j.matbio.2010.10.001 Medline
- 40. G. Zhang, Y. Ezura, I. Chervoneva, P. S. Robinson, D. P. Beason, E. T. Carine, L. J. Soslowsky, R. V. Iozzo, D. E. Birk, Decorin regulates assembly of collagen fibrils and acquisition of biomechanical properties during tendon development. J. Cell. Biochem. 98, 1436-1449 (2006). doi:10.1002/jcb.20776
- 41. S. P. Reese, C. J. Underwood, J. A. Weiss, Effects of decorin proteoglycan on fibrillogenesis, ultrastructure, and mechanics of type I collagen gels. Matrix Biol. 32, 414-423 (2013). doi:10.1016/j.matbio.2013.04.004 Medline
- 42. I. M. Reichardt, K. Z. Robeson, M. Regnier, J. Davis, Controlling cardiac fibrosis through fibroblast state space modulation. Cell. Signal. 79, 109888 (2021). doi:10.1016/j.cellsig.2020.109888 Medline
- 43. M. D. Tallquist, J. D. Molkentin, Redefining the identity of cardiac fibroblasts. Nat. Rev. Cardiol. 14, 484-491 (2017). doi:10.1038/nrcardio.2017.57 Medline
- 44. D. Bugg, L. R. J. Bailey, R. C. Bretherton, K. E. Beach, I. M. Reichardt, K. Z. Robeson, A. C. Reese, J. Gunaje, G. Flint, C. A. DeForest, A. Stempien-Otero, J. Davis, MBNL1 drives dynamic transitions between fibroblasts and myofibroblasts in cardiac wound healing. Cell Stem Cell 29, 419-433.e10 (2022). doi:10.1016/j.stem.2022.01.012 Medline
- 45. J. Davis, N. Salomonis, N. Ghearing, S.-C. J. Lin, J. Q. Kwong, A. Mohan, M. S. Swanson, J. D. Molkentin, MBNL1-mediated regulation of differentiation RNAs promotes myofibroblast transformation and the fibrotic response. Nat. Commun. 6, 10084 (2015). doi:10.1038/ncomms10084 Medline
- 46. J. D. Molkentin, D. Bugg, N. Ghearing, L. E. Dorn, P. Kim, M. A. Sargent, J. Gunaje, K. Otsu, J. Davis, Fibroblast-Specific Genetic Manipulation of p38 Mitogen-Activated Protein Kinase In Vivo Reveals Its Central Regulatory Role Fibrosis. Circulation 549-561 (2017).

First release: 11 September 2025

- doi:10.1161/CIRCULATIONAHA.116.026238 Medline
- 47. L. Hortells, I. Valiente-Alandi, Z. M. Thomas, E. J. Agnew, D. J. Schnell, A. J. York, R. J. Vagnozzi, E. C. Meyer, J. D. Molkentin, K. E. Yutzey, A specialized population of Periostin-expressing cardiac fibroblasts contributes to postnatal cardiomyocyte maturation and innervation. Proc. Natl. Acad. Sci. U.S.A. 117, 21469-21479 (2020). doi:10.1073/pnas.2009119117 Medline
- 48. S. Checa, M. K. Rausch, A. Petersen, E. Kuhl, G. N. Duda, The emergence of extracellular matrix mechanics and cell traction forces as important regulators of cellular self-organization. Biomech. Model. Mechanobiol. 14, 1-13 (2015). doi:10.1007/s10237-014-0581-9 Medline
- 49. K. S. Bielawski, A. Leonard, S. Bhandari, C. E. Murry, N. J. Sniadecki, Real-Time Force and Frequency Analysis of Engineered Human Heart Tissue Derived from Induced Pluripotent Stem Cells Using Magnetic Sensing. Tissue Eng. Part C Methods 22, 932-940 (2016). doi:10.1089/ten.tec.2016.0257 Medline
- 50. P. Mulimani, N. A. Mazzawi, A. J. Goldstein, A. M. Obenaus, S. M. Baggett, D. Truong, T. E. Popowics, N. J. Sniadecki, Engineered 3D Periodontal Ligament Model with Magnetic Tensile Loading. J. Dent. Res. 103, 1008–1016 (2024). doi:10.1177/00220345241264792 Medline
- 51. Y. Xiao, M. C. Hill, L. Li, V. Deshmukh, T. J. Martin, J. Wang, J. F. Martin, Hippo pathway deletion in adult resting cardiac fibroblasts initiates a cell state transition with spontaneous and self-sustaining fibrosis. Genes Dev. 33, 1491-1505 (2019). doi:10.1101/gad.329763.119 Medline
- 52. Y. Xiao, M. C. Hill, M. Zhang, T. J. Martin, Y. Morikawa, S. Wang, A. R. Moise, J. D. Wythe, J. F. Martin, Hippo Signaling Plays an Essential Role in Cell State Transitions during Cardiac Fibroblast Development. Dev. Cell 45, 153-169.e6 (2018). doi:10.1016/j.devcel.2018.03.019 Medline
- 53. K. C. Lin, T. Moroishi, Z. Meng, H.-S. Jeong, S. W. Plouffe, Y. Sekido, J. Han, H. W. Park, K.-L. Guan, Regulation of Hippo pathway transcription factor TEAD by p38 MAPK-induced cytoplasmic translocation. *Nat. Cell Biol.* **19**, 996–1002 (2017). doi:10.1038/ncb3581 Medline
- 54. D. Bugg, R. Bretherton, P. Kim, E. Olszewski, A. Nagle, A. E. Schumacher, N. Chu, J. Gunaje, C. A. DeForest, K. Stevens, D.-H. Kim, J. Davis, Infarct Collagen Topography Regulates Fibroblast Fate via p38-Yes-Associated Protein Transcriptional Enhanced Associate Domain Signals, Circ. Res. 127, 1306–1322 (2020). doi:10.1161/CIRCRESAHA.119.316162 Medline
- 55. S. Bhattacharyya, F. Fang, W. Tourtellotte, J. Varga, Egr-1: New conductor for the tissue repair orchestra directs harmony (regeneration) or cacophony (fibrosis). J. Pathol. 229, 286-297 (2013). doi:10.1002/path.4131 Medline
- 56. L. M. Khachigian, Early Growth Response-1, an Integrative Sensor in Cardiovascular and Inflammatory Disease. J. Am. Heart Assoc. 10, e023539 (2021). doi:10.1161/JAHA.121.023539 Medline
- 57. L. Zhang, J. Elkahal, T. Wang, R. Rimmer, A. Genzelinakh, E. Bassat, J. Wang, D. Perez, D. Kain, D. Lendengolts, R. Winkler, H. Bueno-Levy, K. B. Umansky, D. Mishaly, A. Shakked, S. Miyara, A. Sarusi-Portuguez, N. Goldfinger, A. Prior, D. Morgenstern, Y. Levin, Y. Addadi, B. Li, V. Rotter, U. Katz, E. M. Tanaka, V. Krizhanovsky, R. Sarig, E. Tzahor, Egr1 regulates regenerative senescence and cardiac repair. Nat. Cardiovasc. Res. 3, 915-932 (2024). doi:10.1038/s44161-024-00493-1 Medline
- 58. C. J. Chan, C. P. Heisenberg, T. Hiiragi, Coordination of Morphogenesis and Cell-Fate Specification in Development. Curr. Biol. 27, R1024-R1035 (2017). doi:10.1016/j.cub.2017.07.010 Medline
- 59. D. Gilmour, M. Rembold, M. Leptin, From morphogen to morphogenesis and back. Nature 541, 311-320 (2017). doi:10.1038/nature21348 Medline
- 60. C. P. Heisenberg, Y. Bellaïche, Forces in tissue morphogenesis and patterning. Cell 153, 948-962 (2013). doi:10.1016/j.cell.2013.05.008 Medline
- 61. N. I. Petridou, Z. Spiró, C. P. Heisenberg, Multiscale force sensing in development. Nat. Cell Biol. 19, 581-588 (2017). doi:10.1038/ncb3524
- 62. M. Pesce, G. N. Duda, G. Forte, H. Girao, A. Raya, P. Roca-Cusachs, J. P. G. Sluijter, C. Tschöpe, S. Van Linthout, Cardiac fibroblasts and mechanosensation in heart development, health and disease. Nat. Rev. Cardiol. 20, 309-324 (2023). doi:10.1038/s41569-022-00799-2 Medline
- 63. A. G. Rodriguez, S. J. Han, M. Regnier, N. J. Sniadecki, Substrate stiffness increases twitch power of neonatal cardiomyocytes in correlation with

- changes in myofibril structure and intracellular calcium. Biophys. J. 101, 2455-2464 (2011). doi:10.1016/j.bpj.2011.09.057 Medline
- 64. X. Fu, H. Khalil, O. Kanisicak, J. G. Boyer, R. J. Vagnozzi, B. D. Maliken, M. A. Sargent, V. Prasad, I. Valiente-Alandi, B. C. Blaxall, J. D. Molkentin, Specialized fibroblast differentiated states underlie scar formation in the infarcted mouse heart. J. Clin. Invest. 128, 2127–2143 (2018). doi:10.1172/JCI98215 Medline
- 65. M. J. Ivey, J. T. Kuwabara, K. L. Riggsbee, M. D. Tallquist, Platelet-derived growth factor receptor- α is essential for cardiac fibroblast survival. Am. J. Heart Circ. Physiol. 317, H330-H344 doi:10.1152/ajpheart.00054.2019 Medline
- 66. J. T. Kuwabara, A. Hara, S. Bhutada, G. S. Gojanovich, J. Chen, K. Hokutan, V. Shettigar, A. Y. Lee, L. P. DeAngelo, J. R. Heckl, J. R. Jahansooz, D. K. Tacdol, M. T. Ziolo, S. S. Apte, M. D. Tallquist, Consequences of PDGFR α^+ fibroblast reduction in adult murine hearts. eLife 11, e69854 (2022). doi:10.7554/eLife.69854 Medline
- 67. T. R. Eijgenraam, H. H. W. Silljé, R. A. de Boer, Current understanding of fibrosis in genetic cardiomyopathies. Trends Cardiovasc. Med. 30, 353-361 (2020). doi:10.1016/j.tcm.2019.09.003 Medline
- 68. J. Davis, M. Maillet, J. M. Miano, J. D. Molkentin, Lost in transgenesis: A user's guide for genetically manipulating the mouse in cardiac research. Circ. Res. 111, 761-777 (2012). doi:10.1161/CIRCRESAHA.111.262717 Medline
- 69. J. S. Bredfeldt, Y. Liu, M. W. Conklin, P. J. Keely, T. R. Mackie, K. W. Eliceiri, Automated quantification of aligned collagen for human breast carcinoma prognosis. J. Pathol. Inform. 5, 28 (2014). doi:10.4103/2153-3539.139707 Medline
- 70. Y. Liu, A. Keikhosravi, G. S. Mehta, C. R. Drifka, K. W. Eliceiri, Methods for Quantifying Fibrillar Collagen Alignment. Methods Mol. Biol. 1627, 429-451 (2017). doi:10.1007/978-1-4939-7113-8_28 Medline
- 71. M. Pachitariu, M. Rariden, C. Stringer, Cellpose-SAM: superhuman generalization for cellular segmentation. bioRxiv 2025.04.28.651001 [Preprint] (2025); https://doi.org/10.1101/2025.04.28.651001.
- 72. A. Dobin, C. A. Davis, F. Schlesinger, J. Drenkow, C. Zaleski, S. Jha, P. Batut, M. Chaisson, T. R. Gingeras, STAR: Ultrafast universal RNA-seq aligner. Bioinformatics 29, 15-21 (2013). doi:10.1093/bioinformatics/bts635 Medline
- 73. Y. Liao, G. K. Smyth, W. Shi, featureCounts: An efficient general purpose program for assigning sequence reads to genomic features. Bioinformatics 30, 923-930 (2014). doi:10.1093/bioinformatics/btt656 Medline
- 74. M. I. Love, W. Huber, S. Anders, Moderated estimation of fold change and dispersion for RNA-seq data with DESeq2. Genome Biol. 15, 550 (2014). doi:10.1186/s13059-014-0550-8 Medline
- 75. U. Raudvere, L. Kolberg, I. Kuzmin, T. Arak, P. Adler, H. Peterson, J. Vilo, g:Profiler: a web server for functional enrichment analysis and conversions of gene lists (2019 update). Nucleic Acids Res. 47 (W1), W191-W198 (2019). doi:10.1093/nar/gkz369 Medline
- 76. B. K. Martin, C. Qiu, E. Nichols, M. Phung, R. Green-Gladden, S. Srivatsan, R. Blecher-Gonen, B. J. Beliveau, C. Trapnell, J. Cao, J. Shendure, Optimized single-nucleus transcriptional profiling by combinatorial indexing. Nat. Protoc. 18, 188-207 (2023). doi:10.1038/s41596-022-00752-0 Medline
- 77. L. R. J. Bailey, D. Bugg, I. M. Reichardt, C. D. Ortaç, A. Nagle, J. Gunaje, A. Martinson, R. Johnson, M. J. MacCoss, T. Sakamoto, D. P. Kelly, M. Regnier, J. Davis, MBNL1 Regulates Programmed Postnatal Switching Between Regenerative and Differentiated Cardiac States. Circulation 149, 1812–1829 (2024). doi:10.1161/CIRCULATIONAHA.123.066860 Medline
- 78. S. L. Wolock, R. Lopez, A. M. Klein, Scrublet: Computational Identification of Cell Doublets in Single-Cell Transcriptomic Data. Cell Syst. 8, 281-291.e9 (2019). doi:10.1016/j.cels.2018.11.005 Medline
- 79. Y. Hao, S. Hao, E. Andersen-Nissen, W. M. Mauck 3rd, S. Zheng, A. Butler, M. J. Lee, A. J. Wilk, C. Darby, M. Zager, P. Hoffman, M. Stoeckius, E. Papalexi, E. P. Mimitou, J. Jain, A. Srivastava, T. Stuart, L. M. Fleming, B. Yeung, A. J. Rogers, J. M. McElrath, C. A. Blish, R. Gottardo, P. Smibert, R. Satija, Integrated analysis of multimodal single-cell data. Cell 184, 3573-3587.e29 (2021). doi:10.1016/j.cell.2021.04.048 Medline
- 80. A. Butler, P. Hoffman, P. Smibert, E. Papalexi, R. Satija, Integrating single-cell transcriptomic data across different conditions, technologies, and species.

First release: 11 September 2025

- Nat. Biotechnol. 36, 411-420 (2018). doi:10.1038/nbt.4096 Medline
- 81. B. Hegyi, J. M. Borst, L. R. J. Bailey, E. Y. Shen, A. J. Lucena, M. F. Navedo, J. Bossuyt, D. M. Bers, Hyperglycemia regulates cardiac K+ channels via O-GlcNAc-CaMKII and NOX2-ROS-PKC pathways. Basic Res. Cardiol. 115, 71 (2020). doi:10.1007/s00395-020-00834-8 Medline
- 82. S. Bremner, A. J. Goldstein, T. Higashi, N. J. Sniadecki, Engineered Heart Tissues for Contractile, Structural, and Transcriptional Assessment of Human Pluripotent Stem Cell-Derived Cardiomyocytes in a Three-Dimensional, Auxotonic Environment. Methods Mol. Biol. 2485, 87-97 (2022). doi:10.1007/978-1-0716-2261-2 6 Medline

ACKNOWLEDGMENTS

We acknowledge the support of the proteomics and bioinformatics core of the Diabetes Research Center NIDDK (DK017047), D. Hailey and the Garvey Imaging core at the UW Institute for Stem Cell and Regenerative Medicine (ISCRM), and B. Johnson and the UW Histology and Imaging Core. We thank R. Tian for use of critical instrumentation, S. Mohran for insightful discussion, and E. Olszewski and other members of the Davis lab for their insights and experimental assistance. Funding: We acknowledge funding from ISCRM (fellowship to R.C.B.), the German Research Foundation (Li 690/14-1 to W.A.L.), the National Science Foundation (DGE 1762114 to R.C.B. and I.M.R.), and the National Institutes of Health (FHL 165834A to I.M.R.; P30 AR074990 to N.J.S. and M.R.; R01 HL149734 and R01 HL146868 to N.J.S.; RM1 GM131981 to M.R.; R01 HL.157169 to F.M.-H.; R35 GM138036 to C.A.D.; R01 HL142624, HL141187, and HL162229 to J.D.). Author contributions: R.C.B., I.M.R., K.A.Z., A.N., A.L.G., L.R.J.B., D.B., S.S., A.J.G., T.S.M., K.B.K., G.V.F., A.M., J.G., F.K., E.P., W.A.L., and J.D. performed experiments and analyzed results. R.C.B., I.M.R., K.A.Z., T.S.M., K.B.K., W.L., M.R., F.M.-H., N.J.S., C.A.D, and J.D. conceived the experiments. R.C.B., M.R., N.J.S., C.A.D., and J.D. wrote and reviewed the manuscript. Competing interests: R.C.B. is affiliated with Research & Early Development at Novo Nordisk A/S, but this affiliation is not relevant to the work presented in this article. The rest of the authors declare that they have no competing interests. Data and materials availability: All sequencing data in the study are freely available and deposited at Gene Expression Omnibus (GEO) repository. The GEO accession number is GSE294563. GSM8911388 to GSM8911399 were the accession numbers assigned to each of the individual data files. Other data are available in the main text or supplementary material. License information: Copyright © 2025 the authors, some rights reserved; exclusive licensee American Association for the Advancement of Science. No claim to original US government works. https://www.science.org/about/science-licensesjournal-article-reuse

SUPPLEMENTARY MATERIALS

science.sciencemag.org/cgi/content/full/science.adv9157/DC1 Figs. S1 to S6 Tables S1 to S3 MDAR Reproducibility Checklist

Submitted 12 January 2025; accepted 06 August 2025 Published online 11 September 2025 10.1126/science.adv9157

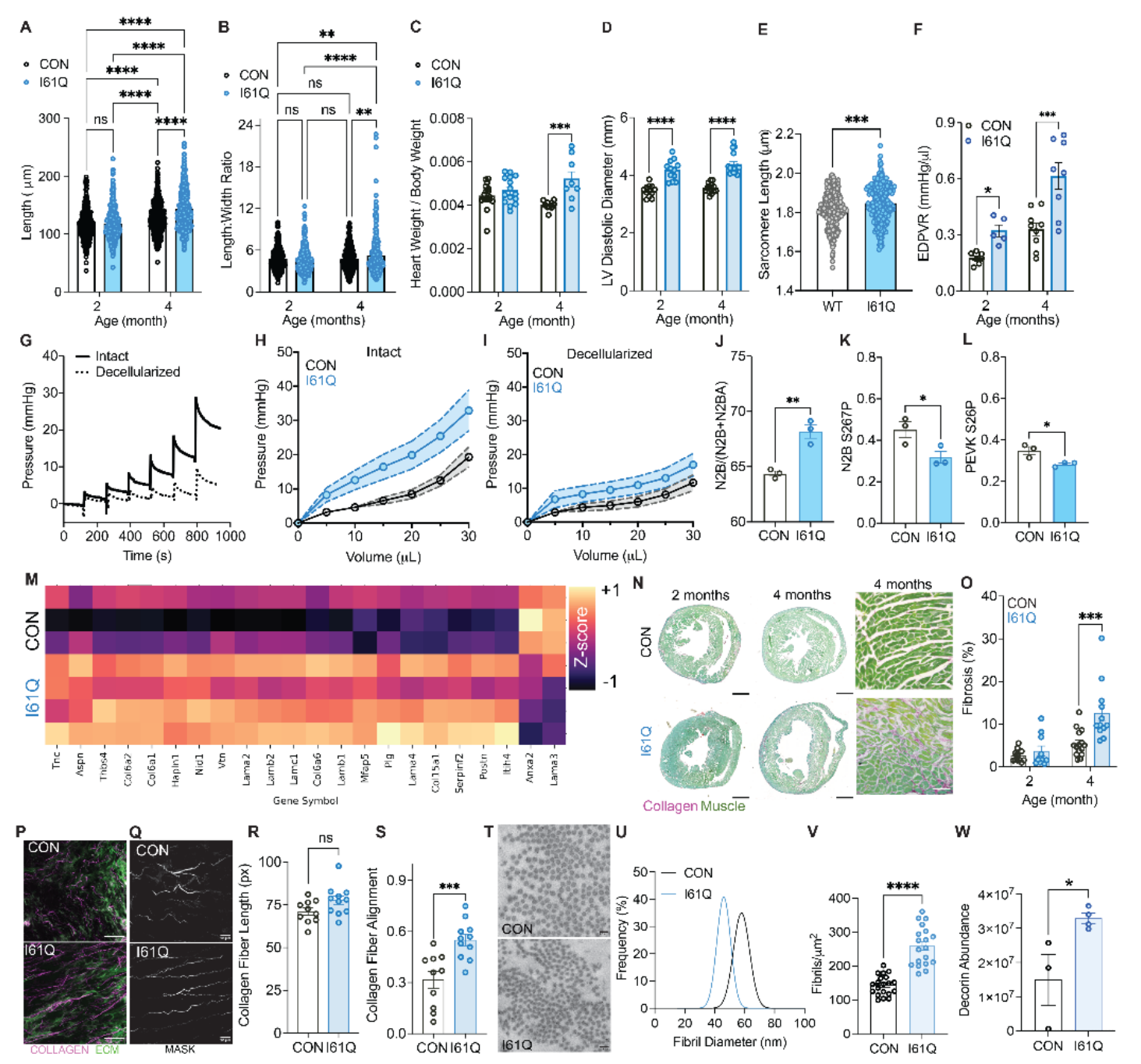


Fig. 1. Cardiomyocyte hypocontractility stiffens and aligns the myocardium prior to eccentric hypertrophic remodeling and fibrosis. (A) Quantification of isolated cardiomyocyte length and (B) length: width ratio in relaxed conditions from the described genotypes [CON n=399/402 (2/4 month), I61Q n=357/399 (2/4 month)]. Quantification of (C) heart weight to body weight ratio by gravimetrics and (D) left ventricular diastolic chamber diameter by echocardiography at 2 (I61Q n=12, CON n=12) and 4 (I61Q n=16, CON n=15) months of age. (E) Quantification of diastolic sarcomere length in intact cardiomyocytes from I61Q and CON hearts [CON n=399/402 (2/4 month), I61Q n=357/399 (2/4 month)]. (F) Quantification of EDPVR by invasive hemodynamics [CON n=5/9 (2/4 month), I61Q n=5/8 (2/4 month)]. (G) Representative developed pressure traces from stepwise inflation of a balloon inside a blebbistatin-treated intact (black line) and decellularized (dotted line) heart. Pressure-volume curves of (H) intact and (I) decellularized mouse hearts at 2 months (n=7 both genotypes). Quantification of titin (J) isoforms N2B and N2BA, (K) N2B S267 phosphorylation site, and (L) serine PEVK region S267 phosphorylation by Coomassie staining and Western blot (n=3 both genotypes). N2B isoform is expressed relative to the total titin (N2B + N2BA) and phosphospecific antibodies were normalized to the titin stain on the Coomassie gel. (M) Heatmap of differentially expressed matrisome proteins color coded by z-score identified by MS in 2-month-old decellularized ECM (CON n=3, I61Q n=4). (N) Representative images and (O) quantification of fibrosis in cardiac sections stained with picrosirius red-fast green (PSR/FG, scale bar = 1 mm (left and middle panel), scale bar = 50 μm (right panel)). (P) Representative two-photon max intensity projection images of SHG (left panel, scale bar = 100 µm) and (Q) masking of the collagen fibers (scale bar = $20 \mu m$) in decellularized hearts in which Z-stacks were taken starting 10 micron below the epicardial surface. Fibrillar collagen (magenta) and ECM autofluorescence (green). CurveAlign quantification of collagen fiber (R) length and (S) alignment from 2-month-old I61Q (n=10) and CON (n=11) hearts. (T) Representative TEM images of collagen fibrils in 2-month-old I61Q and CON hearts. Quantification of (U) fibril diameter and (V) density from TEM images (n=20 ROIs/mouse, 3 mice per genotype). (W) Quantification of decorin abundance identified by MS. [(A), (B), and (E)] Four biological replicates per genotype were used for isolated myocyte experiments. Data are mean ± SEM. ns, not significant; **P < 0.01; ***P < 0.005; ****P < 0.001 by two-way ANOVA with Holm-Sidak's multiple comparisons test [(A) to (D), (F), and (O)] or two-tailed unpaired t test [(E), (J) to (L), (R), (S), (V), and (W)].

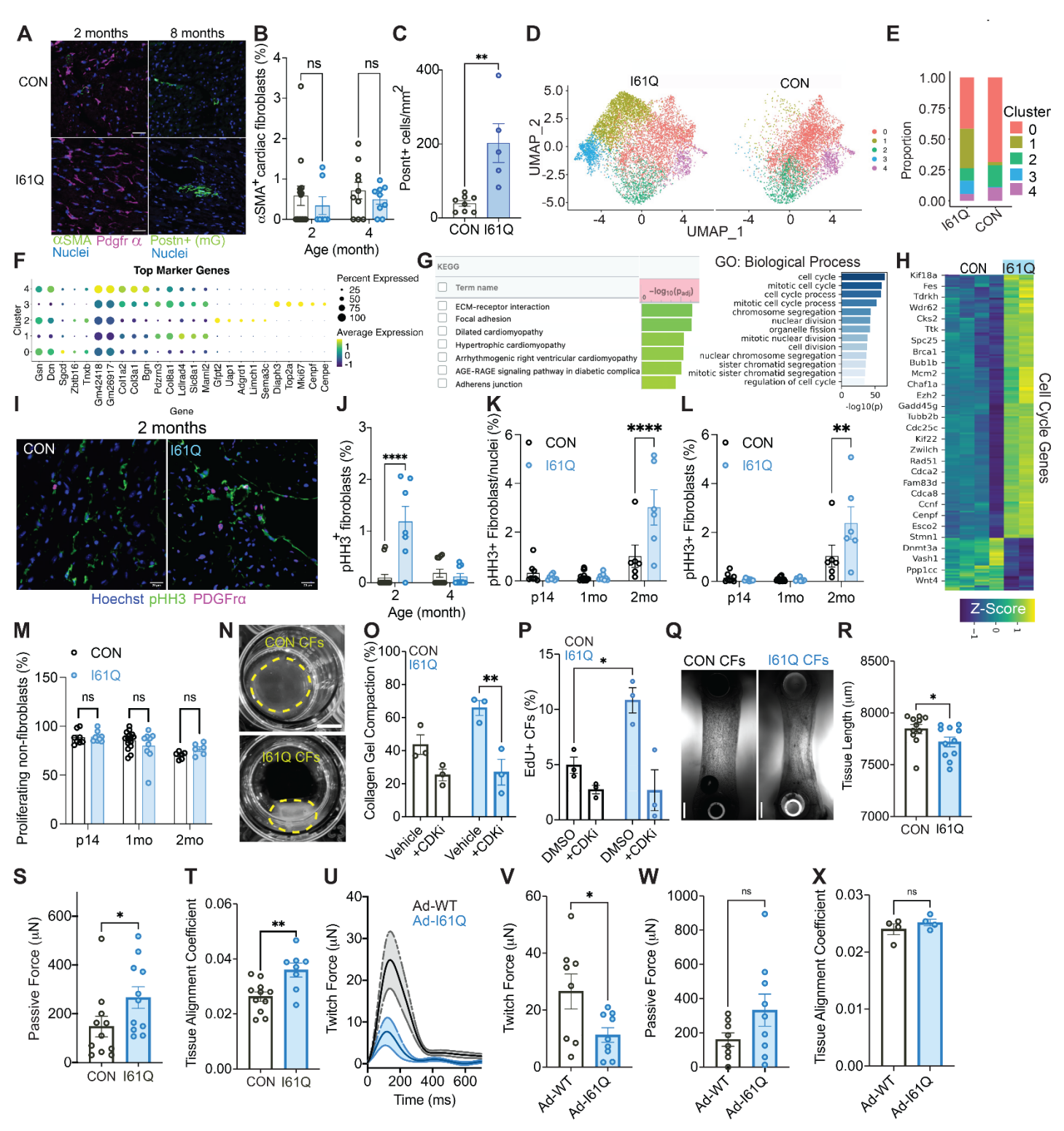


Fig. 2. Hyperproliferative fibroblast states drive fibrosis-independent tissue stiffening in I61Q hearts. (A) Representative images of (Left) 2-month-old CON and I61Q cardiac sections stained for αSMA and platelet-derived growth factor receptor α (PDGFRα) and (Right) Postn lineage traced cell density in 8-month-old cardiac sections. (B) Quantification of immunofluorescent imaging for the percentage of fibroblasts (PDGFR α^+) expressing α SMA (2 month n=14 CON, n=7 I61Q, 4 month n=10 CON, n=9 I61Q). (C) Quantification of Postn⁺ cell density in I61Q (n=5) and CON (n=8) hearts at 8 months of age. (D) UMAP dimensionality reduction plot for all sequenced cardiac fibroblast nuclei from 2-month-old I61Q and CON hearts. Each color represents distinct fibroblast clusters (states) based on differential gene expression. (E) Proportion analysis showing genotype-dependent changes in the percentage of the cardiac fibroblast population residing in each of the defined cell clusters (states). (F) Dot plot of the top five expressed genes that define each fibroblast cluster. (G) Kegg pathways and gene ontology biological processes (GO:BP) identified by differentially regulated genes in fibroblast clusters 1 and 3 that are specific to the I61Q genotype. (H) Heatmap showing expression levels of cell cycle genes. (I) Representative images (scale bar = 20 μm) and quantification of immunofluorescent staining for: (J) phospho-histone H3 (pHH3) and PDGFRα, (K) pHH3+, PDGFRα+ cells per total nuclei (Hoechst), and (L) pHH3+, PDGFR α + cells as a percentage of the total number of PDGFR α + cells in I61Q and CON cardiac sections. (M) Quantification of pHH3+ non fibroblasts in I61Q [n=8 (p14), 9 (1 month), 6 (2 month)] and CON [n=8 (p14), 15 (1 month), 6 (2 month)] cardiac sections. (N) Representative images (scale bar = 5 mm) and (O) quantification of the compaction of free-floating collagen gels seeded with cardiac fibroblasts (CFs) isolated from I61Q and CON hearts ± cell cycle inhibitor (CDKi, dinaciclib, 5 μM); n=5 per genotype. (P) Quantification of cardiac fibroblast proliferation by EdU incorporation ± cell cycle inhibitor (CDKi, dinaciclib, 5 μM). (Q) Representative images of fibrin tissues seeded with cardiac fibroblasts mounted between posts (scale bar = 1 mm). Quantification of (R) length and (S) passive force production by tissues seeded with cardiac fibroblasts from 2-month-old I61Q cTnC transgenic or CON mice (n=11 per genotype). (T) Quantification of cellular and ECM alignment in fibrin tissues seeded with cardiac fibroblasts derived from I61Q cTnC transgenic and CON hearts by wheat germ staining (n=11 CON, n=8 I61Q). (U) Average twitch forces generated by engineered heart tissues (EHTs) 2 weeks after cardiomyocytes were adenovirally transduced with either control (AdWT, n=8) or I61Q mutant cTnC (AdI61Q, n=6). Quantification of (V) twitch force, (W) passive tension, and (X) tissue alignment by wheatgerm staining in EHTs. Data are mean \pm SEM. ns, not significant; *P < 0.05; ***P < 0.01; ****P < 0.005; ****P < 0.005; *****P < 0.005; ****P < 0.005; *****P < 0.005; *****P < 0.005; *****P < 0.005; *****P < 0.005; ****P < 0.005; *****P < 0.005; *****P < 0.005; ****P < 0.005; ****P < 0.005; *****P < 0.005; ****P < 0.005; *****P < 0.005; ****P < 0.005; *****P < 0.005; ****P < 0.005; *****P < 0.005; ******P < 0.005; *****P < 0.005; *****P < 0.005; ******P < 0.005two-way ANOVA with Holm-Sidak's multiple comparisons test [(B), (J) to (M), (O), and (P)] or two-tailed unpaired t test [(C), (R) to (T), and (V) to (X)]. All scale bars are 50 μm unless otherwise noted.

science.org

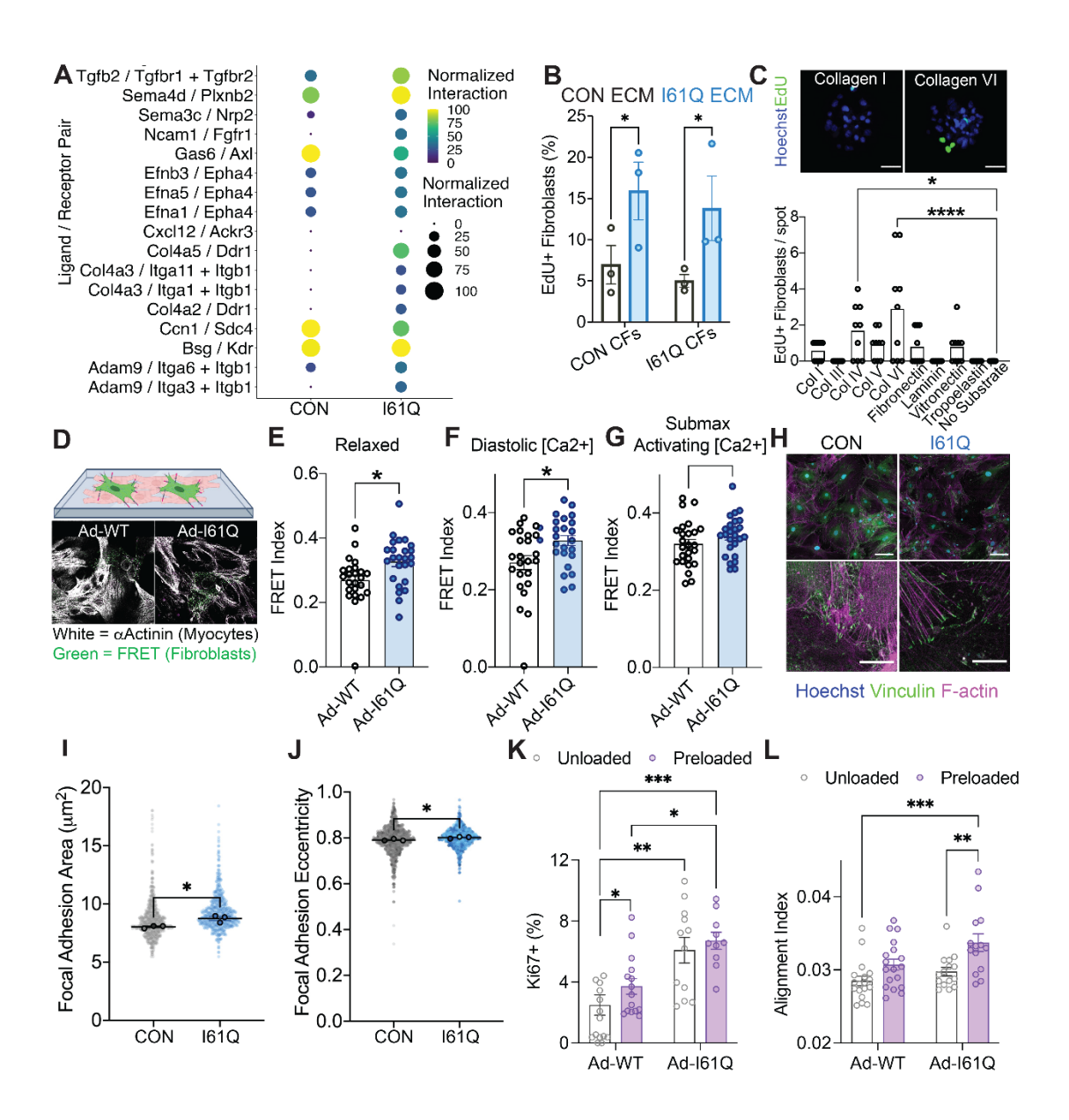


Fig. 3. Diastolic mechanosensations at fibroblast focal adhesions are accentuated by ECM-receptor interactions that trigger proliferation. (A) Ligand-receptor analysis of myocyte-fibroblast interactions predicted from snRNA-seq of 2-month-old CON and I61Q hearts where the ligand is expressed in myocytes and receptor is expressed in fibroblasts. (B) Proliferation by EdU assay of CON and I61Q fibroblasts seeded within PEG gels decorated with ECM peptides from CON and I61Q hearts. (C) (Top) Representative images of cardiac fibroblasts seeded onto the ECM screening array stained for EdU to mark proliferating cells (scale bar = 100 μm) and (bottom) quantification of EdU+ fibroblast counts on ECM-coated microspots. (D) Schematic of cocultures with cardiomyocyte monolayers adenovirally transduced with either CON or I61Q cTnC that were sparsely overlaid with cardiac fibroblasts genetically encoded with a FRET-tension sensor in the focal adhesion protein vinculin. Quantification of the average FRET efficiency (correlates with tension) at fibroblast focal adhesions in (E) relaxed (+blebbistatin), (F) diastolic [Ca²⁺], and (G) submaximal activating conditions (n=25 fibroblasts per group). (H) Representative images (top scale bar =100 μm, bottom scale bar = 30 μm) of CON and I61Q cardiac fibroblasts stained for vinculin and filamentous actin (F-actin) and quantified for focal adhesion (I) area and (J) eccentricity (n=681 CON and 622 I61Q fibroblasts from 3 different mice per genotype). Quantification of (K) the percentage of proliferating cardiac fibroblast as measured by Ki67 positivity (n=15 unloaded-WT, n=15 preloaded-WT, n=15 unloaded-I61Q, n=15 preloaded-I61Q) and (L) collagen alignment (n=18 unloaded-WT, n=18 preloaded-WT, n=15 unloaded-I61Q, n=14 preloaded-I61Q) in unloaded or chronically preloaded EHTs generated with cardiomyocytes adenovirally transduced with WT or I61Q cTnC. *P < 0.05; **P < 0.01; ***P < 0.005 by either two-way or one-way ANOVA with Holm-Sidak's multiple comparisons test [(B), (C), (K), and (L)], or two-tailed unpaired t test [(E) to (G), (I), and (J)].

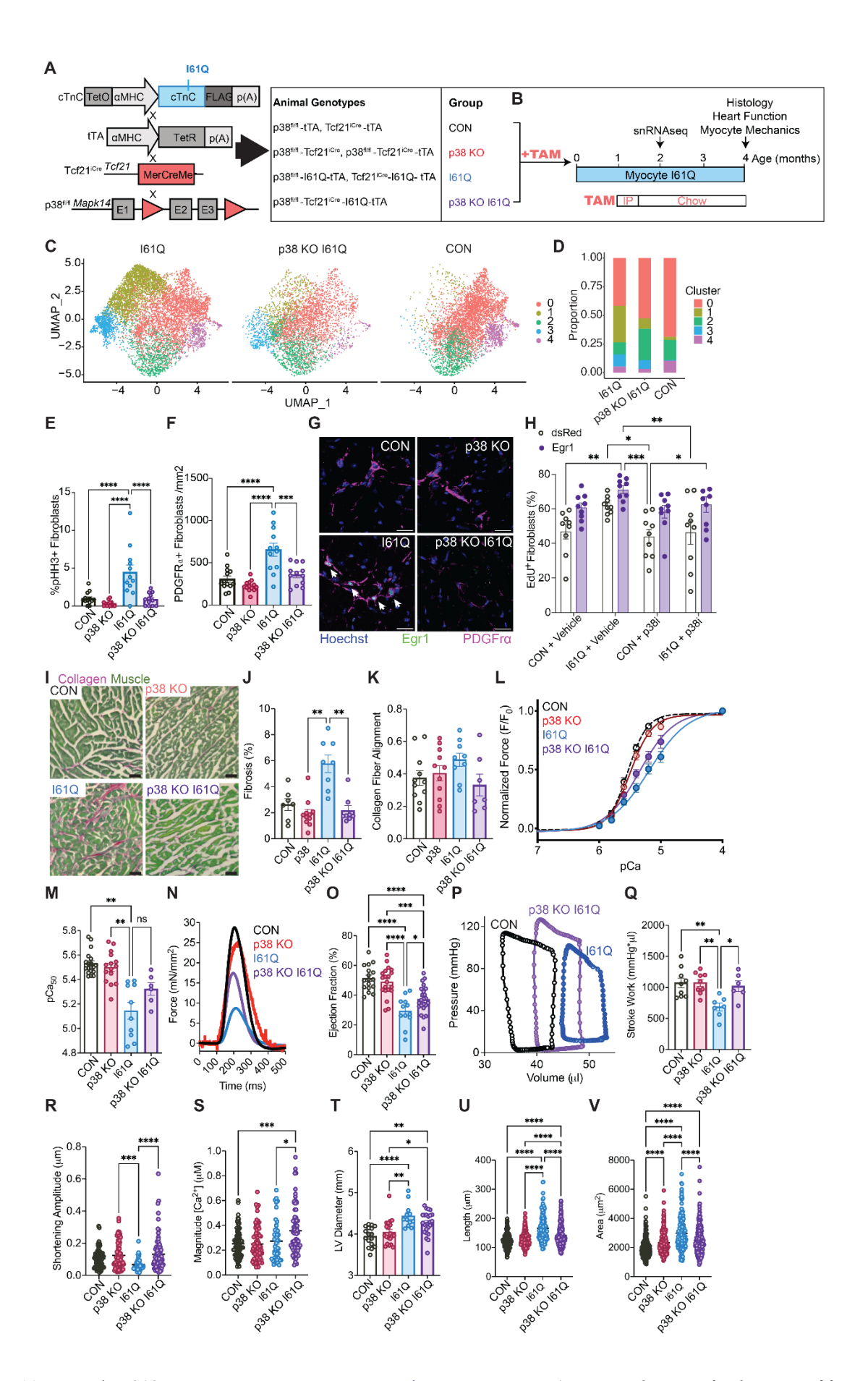


Fig. 4. Fibroblast-specific p38 deficiency corrects cardiac dilation and systolic dysfunction in I61Q cTnC transgenic mice. (A) Schematic showing the generation of I61Q cTnC transgenic mice with tamoxifen-inducible fibroblast-specific p38 deletion and the experimental genotypes derived from the described breeding scheme. Here, I61Q cTnC and tTA transgenic animals were bred with a mouse line containing conditional p38 α loss of function (p38 $^{\mathrm{fl/fl}}$) and a tamoxifen-inducible Cre recombinase knocked into the Tcf21 locus (Tcf21^{iCre}). (B) Experimental design schematic showing that the I61Q mutant cTnC was expressed just after birth (~ postnatal day 2), mice were allowed to develop normally for 1 month, and then tamoxifen was administered to induce fibroblastspecific p38 excision. Experimental endpoints were at 2 and 4 months of age. (C) UMAP dimensionality reduction plot and (D) proportion analysis for all sequenced cardiac fibroblast nuclei from 2-month- old I61Q, p38-I61Q, and CON hearts. Each color represents distinct fibroblast clusters (states) based on differential gene expression. UMAPs for I61Q and CON were also shown in Fig. 2 for clarity, but all three groups were sequenced simultaneously as part of the same experiment. Quantification of (E) fibroblast proliferation and (F) fibroblast density by immunofluorescent staining for pH3 and PDGFRα in 2-month-old myocardial sections (CON n=13, p38KO n=13, I61Q n=12, p38KO-I61Q n=12). (G) Representative images of EGR1 (green) and PDGFRα (magenta) in myocardial sections. White arrows indicate EGR1+ nuclei (Hoescht stain, CON n=8, p38KO n=8, I61Q n=7, p38KO-l61Q n=7; scale bar = 100 μm). (H) Quantification of the percentage of proliferating CON or I61Q cardiac fibroblasts ± dsRed (control) or human EGR1 retroviral vectors ± p38 inhibitor as determined by EdU positivity (EdU+). (I) Representative PSR/FG stained myocardial sections (scale bars = 50 μm) and (J) quantification of collagen (red) (CON n=7, p38KO n=11, l61Q n=8, p38KO-l61Q n=8). (K) Quantification of collagen fiber alignment from decellularized CON (n=11), p38KO (n=11), l61Q (n=9), and p38KO-l61Q (n=7) hearts. (L) Representative relationship between normalized tension and Ca²⁺ concentration (pCa) and (M) Ca²⁺ sensitivity of tension generation (pCa₅₀) in membrane permeabilized trabeculae of CON (n=19), p38KO (n=15), l61Q (n=10), and p38KO-l61Q (n=6) mice. (N) Mean twitch forces from intact trabeculae of 4-month-old CON (n=5), p38KO (n=5), l61Q (n=5), and p38KO-l61Q (n=4) mice. (O) Quantification of left ventricular ejection fraction measured by echocardiography from CON (n=17), p38KO (n=20), I61Q (n=12), and p38KO-I61Q (n=23) mice. (P) Representative pressure-volume loops and (Q) quantification of stroke work from invasive hemodynamic measurements at 4 months (CON n=9, p38KO n=9, l61Q n=7, p38KO-l61Q n=6). (R) Quantification of unloaded sarcomere shortening amplitude (CON n=85, p38KO n=87, I61Q n=45, p38KO-I61Q n=85 cardiomyocytes) and (S) Ca²⁺ transient amplitude (CON n=75, p38KO n=81, I61Q n=54, p38KO-I61Q n=66) in isolated intact cardiomyocytes from the described genotypes. (T) Quantification of left ventricular diastolic diameter at 4 months of age by echocardiography [n was the same as in (O)]. (U) Quantification of isolated cardiomyocyte length and (V) area from the described genotypes (CON n=250, p38KO n=250, l61Q n=199, p38KO-I61Q n=200). For isolated myocyte experiments [(R), (S), (U), and (V)], the following biological replicates per genotype were used: CON n=4, p38KO n=5, l61Q n=4, and p38KO-l61Q n=5. Data are mean \pm SEM. ns, not significant; *P < 0.05; **P < 0.01; ***P < 0.005; ****P < 0.001 by two-way ANOVA with Holm-Sidak's multiple comparisons test.